A European endeavor for optimizing Zonal Isolation, Drilling and Exploitation of EGS projects

REPORT AND COMPARATIVE RESULTS OF TASK 3.5

Authors: Víctor Vilarrasa and Jesus Carrera (CSIC); Andres Alcolea and Peter Meier (Geo-Energie Suisse AG)

Date: January 2022

The GEOTHERMICA is supported by the European Union's HORIZON 2020 programme for research, technological development and demonstration under grant agreement No 731117

Contents

Figures

1. Introduction

A suite of hydraulic stimulation tests have been performed at the Bedretto Underground Laboratory for Geosciences and Geoenergies (BULGG) to stimulate fractures intersected by drilled wells. This report presents the numerical modeling and interpretation of the hydraulic stimulation performed in wellbore CB1 in January 2020. The modeling approach follows three steps, each one adding complexity to the numerical solution as the simulated processes progressively resemble reality. In the first approach, the permeability of the whole fracture is manually changed with time to calibrate the injection pressure evolution. In the second approach, permeability changes in response to fracture opening following the cubic law, resulting in variable permeability in time and space along the fracture. In these two approaches, the fracture is assumed to behave elastically. In the third approach, an elastoplastic constitutive law with slip weakening and dilatancy is assumed. The fully coupled hydro-mechanical numerical models are implemented using the software Code_Bright (Olivella et al., 1994 and 1996).

2. Methodology

2.1 Geometry, material properties and initial and boundary conditions

The numerical model is a 2D plane-strain inclined plane that contains the boreholes that, in average, dip 42º downwards. The model has a large extension: the whole domain covers around 75 km^2 of the site (Figure 1). The upper boundary includes the central part of the Bedretto gallery. The bottom boundary is at a true vertical depth of 5000 m (-7472.4 m in the inclined model). The major fractures and shear zones identified through borehole logging and geological structural analysis is also included in the model. The mesh also includes the main boreholes (CB1 to CB4, ST1 and ST2) and is highly refined at the closest vicinity of the modelled fractures and the boreholes. Overall, the mesh consists of 27248 quadrilateral elements with corresponding 27420 nodes.

Numerical models have been developed based on three approaches. First, a model in which the temporal evolution of the fracture permeability has been manually prescribed to achieve a reasonable fit of the measured pressure evolution at the injection borehole (termed here model I). The fracture has been modelled as an elastic continuum medium with homogeneous hydromechanical properties. However, changes in fracture aperture occur mainly in the vicinity of the injection well as a result of injection overpressures. Hence, the second model (model II) employs the so-called embedded model in which permeability is a function of volumetric strain in the fracture based on the cubic law (Olivella and Alonso, 2008). In this model, fracture permeability varies with distance from the injection well and remains constant and equal to the initial value far away from it, where pressurization has not expanded the fracture. While this approach allows to obtain a good reproduction of the injection pressure at early stages, it fails to provide a good fitting once the fracture reactivates and inelastic strains occur. Thus, to account for permeability enhancement induced by dilatancy due to shear slip of the fracture, we use a viscoplastic constitutive law that includes dilatancy and strength softening (models III and IV). Table 1 summarizes the input values for these models. The rock matrix is a granite with the following properties: Young modulus equal to 46 GPa, Poisson ratio equal to 0.37, porosity of 0.005, and constant intrinsic permeability of $2.\ 5{\cdot}10^{-18}$ m^2.

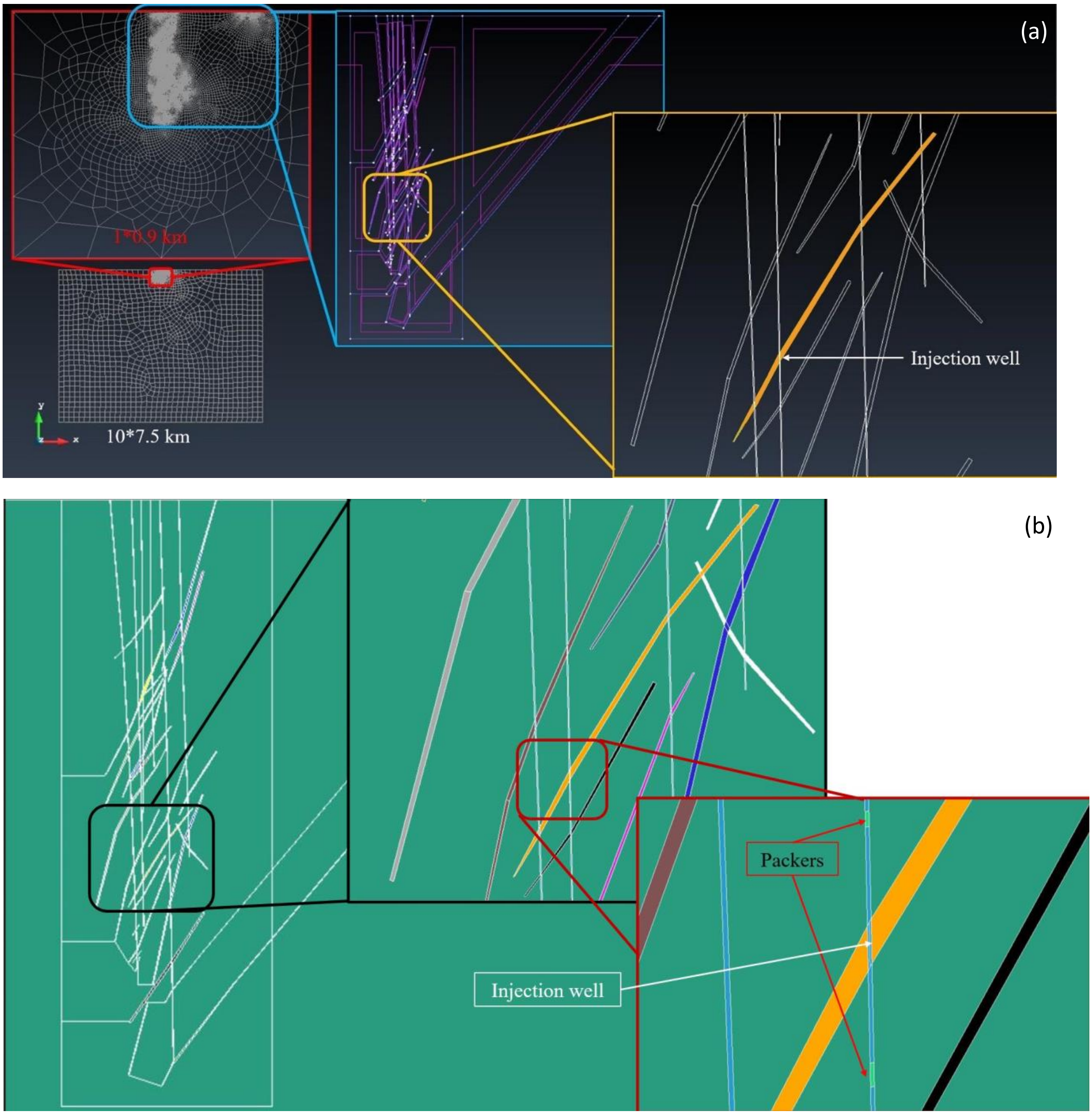

Figure 1. (a) Mesh of the entire model, detail of the refined mesh around the BULGG, geometry including the wellbores and the identified fractures (the stimulated fracture is plot in green), (b) view of the identified fractures and details around the injection interval, including the boreholes (in light blue), the packers (in light green) and the stimulated fracture (in orange).

Table 1. Material properties of the stimulated fracture for models I to IV.

Model	I	II	III	IV
Mechanical behaviour	Elastic		Viscoplastic	
Permeability	Prescribed	Embedded model		
Young´s modulus	23 GPa			
Poisson ratio	0.37			
Viscosity (in the viscoplastic model of the fracture)	-	-	2.5 GPa·s	
Peak friction angle	-	-	23º	23º
Residual friction angle	-	-	23º	20º
Peak & residual cohesion	-	-	0.01 MPa	
Dilatancy angle	-	-	23º	20º
Critical value of the softening parameter (η*)	-	-	0.002	0.001

The models are initialized by simulating the drainage effect of the tunnel on pore pressure and the subsequent consolidation, which tends to close fractures. The drainage period covers 40 years, approximately since the end of the excavation in 1976 until present. Subsequently, the stimulation test is modelled by injecting water through the isolated section of borehole CB1, at a measured depth of 267 m (true vertical depth 188.8 m), into the fracture (in orange in Figure 1a). The numerical simulations cover the first 3.5 hours of the field experiment, during which we compare the simulation and the experimental results. In the following, certain results will be displayed along red line in Figure 2, i.e., at the closest vicinity of the borehole CB1.

Both sides and bottom of the model are fixed against lateral and vertical displacements, respectively. A linear distributed fluid pressure and initial stresses are applied to the model from top to bottom according to Table 2.

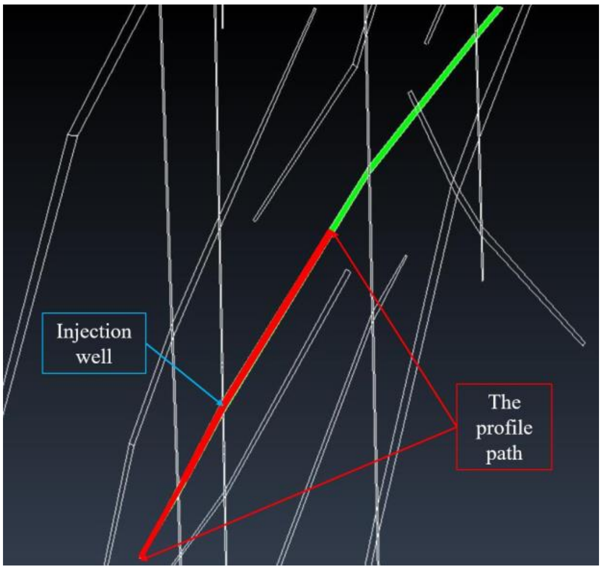

Figure 2. Fracture profile. Results are reported along the red line through the stimulated fracture (in green).

Table 2. Initial stresses and pressure applied to the model

	σ_x (MPa)	σ_y (MPa)	σ_z (MPa)	p_f (MPa)
Top	18.2	20.7	21.8	13.5
Bottom	108.2	124.4	133.3	63.6

2.2 Governing equations

The mechanical problem is solved by satisfying the momentum balance. Neglecting inertial terms, the momentum balance reduces to the equilibrium of stresses,

$$\nabla \cdot \boldsymbol{\sigma} + \boldsymbol{b} = \boldsymbol{0} \tag{1}$$

where $\boldsymbol{\sigma}$ is the total stress tensor and **b** is the vector of body forces.

In linear elasticity theory for continuous media, the relationship between stresses, strain, and fluid pressure for isotropic materials is given by Hooke's law,

$$\Delta\boldsymbol{\sigma} = K\varepsilon_v \boldsymbol{I} + 2G\left(\boldsymbol{\varepsilon} - \frac{\varepsilon_v}{3}\boldsymbol{I} + \frac{\alpha}{2G}\Delta p_f \boldsymbol{I}\right), \tag{2}$$

where ε_v is volumetric strain, $\boldsymbol{I}$ is the identity matrix, ε is the strain tensor, $K = E/\big(3(1-2\nu)\big)$ is the bulk modulus, $G = E/\big(2(1+\nu)\big)$ is the shear modulus, E is Young's modulus, ν is the Poisson ratio, p_f is the fluid pressure, and α is the Biot effective stress coefficient. In this work, we assume $\alpha = 1$, which leads to the strongest hydromechanical coupling (Zimmerman, 2000).

Equation (2) can be coupled with the flow equation through fluid pressure. Assuming that there is no external loading and neglecting the compressibility of the solid phase, fluid mass conservation can be written as

$$\frac{\Phi}{K_f}\frac{\partial p_f}{\partial t} + \frac{d}{dt}(\nabla \cdot \boldsymbol{u}) + \nabla \cdot \boldsymbol{q} = 0, \tag{3}$$

where Φ is porosity, $1/K_f$ is water compressibility, t is time, **u** is the displacement vector and **q** is the water flux, given by Darcy's law. Notice that the flow (Eq. 3) and mechanical (Eq. 2) equations can be also coupled through the volumetric strain (second term in the left-hand side of Eq. 3), which can be expressed as the divergence of the displacement vector.

2.3 Fracture reactivation

Fracture reactivation is modelled by a viscoplastic constitutive law in which failure is given by the Mohr-Coulomb failure criterion and includes dilatancy and strain-softening. The yield function (*F*) and the flow rule (*G*) are defined as

$$F = p \cdot \sin\varphi(\eta) + \left[\cos\theta - \frac{1}{\sqrt{3}}\sin\theta \,.\, \sin\varphi(\eta)\right] \cdot \sqrt{J_2} - c(\eta) \cdot \cos\varphi(\eta)\,, \tag{4}$$

$$G = \xi \cdot p \cdot \sin\psi + \left(\cos\theta - \frac{1}{\sqrt{3}}\sin\theta \cdot \sin\psi\right) \cdot \sqrt{J_2} - c(\eta) \cdot \cos\varphi(\eta)\,, \tag{5}$$

where p is the mean stress, J_2 is the second invariant of the stress tensor, η is the softening parameter, ξ is a parameter for the plastic potential, and ψ is the dilatancy angle. The stress function $\Phi(F)$ is

$$\Phi(F) = F^m \quad for\ F \geq 0 \quad \Phi(F) = 0\ for\ F < 0, \tag{6}$$

where *m* is a constant power, chosen equal to 3 here. Both the cohesion and the friction angle depend on the softening parameter (η) as

$$k(\eta) = \begin{cases} k^{peak} & \eta \leq 0 \\ k^{peak} + \left(\dfrac{k^{res} - k^{peak}}{\eta^*}\right) \cdot \eta & 0 \leq \eta \leq \eta^*, \\ k^{res} & \eta^* \leq \eta \end{cases} \tag{7}$$

where k represents either cohesion (*c*) or friction angle (φ), and k^{peak} and k^{res} are peak and residual values, respectively. Figure 3 represents the variation of *k* based on the softening parameter.

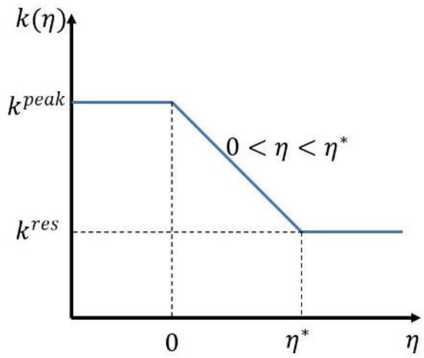

Figure 3. Variation of cohesion and friction angle (denoted as k) as a function of the softening parameter η.

η^* is the value of the softening parameter controlling the transition between the softening and residual stages. The softening parameter depends on plastic strains:

$$\eta = \sqrt{\frac{3}{2} \cdot \left[\left(\varepsilon_x^p - \varepsilon_m^p\right)^2 + \left(\varepsilon_y^p - \varepsilon_m^p\right)^2 + \left(\varepsilon_z^p - \varepsilon_m^p\right)^2 + \left(\frac{1}{2}\gamma_{xy}^p\right)^2 + \left(\frac{1}{2}\gamma_{yz}^p\right)^2 + \left(\frac{1}{2}\gamma_{zx}^p\right)^2 \right]}, \tag{8}$$

where $\varepsilon_m^p = \frac{1}{3}(\varepsilon_x^p + \varepsilon_y^p + \varepsilon_z^p)$, and ε and γ are the diagonal and off-diagonal terms of the plastic strain tensor, respectively.

2.4 The embedded model

Fracture permeability can be computed using the cubic law (Witherspoon et al., 1980), taking into account that aperture changes are a function of volumetric strain as

$$k = k_m + \frac{(b_0 + a\Delta\varepsilon)^3}{12a}, \tag{9}$$

where k_m is the intrinsic permeability of the matrix within the fracture zone (green region in Figure 1b), a is the spacing of the fractures within the fracture zone, b_0 is the initial fracture aperture, $\Delta\varepsilon$ is the volumetric strain change ($\Delta\varepsilon = \varepsilon - \varepsilon_0$), and ε_0 is a threshold value. The input parameters for the embedded model are presented in Table 3. Note that b_{max} is the maximum aperture (upper bound of aperture), above which fracture permeability stops increasing.

Table 3. Parameters used in the embedded model.

k_m (m^2)	Φ	Φ_{min}	b_0 (m)	a (m)	ε_0	b_{max} (m)
$5 \cdot 10^{-17}$	0.005	0.001	$2.25 \cdot 10^{-6}$	0.01	0	$1.34 \cdot 10^{-5}$

3. Results

3.1 Model I with prescribed permeability

The temporal evolution of permeability of the stimulated fracture is manually calibrated in such a way that model outputs reproduce the pressure evolution at the injection well. Although this model yields an overall good fit of measured pressures (Figure 4), it fails to reproduce the shape of the pressure curve in each injection step, in which pressure increases sharply at the beginning but the subsequent pressure build-up diminishes smoothly. In short, model I fits well the begin and end pressures in each step, but not the intermediate evolution. The discrepancy between simulation results and field measurements mainly stems from the fact that permeability changes are prescribed for the whole fracture and not just for the actually stimulated region, which results in a rapid pressure diffusion along the whole fracture (Figure 5). The contour plots of pore pressure at the same the selected times in Figure 5 reveal that adjacent fractures and wellbores start to be pressurized after 2.6 h of stimulation (Figure 6). The pressurization becomes significant outside the stimulated fracture after 3.4 h of stimulation, including the low-permeable rock matrix, which indicates that leak-off is non-negligible and may be responsible of water back-flow into the injection wellbore outside the region between packers (Figure 6e). Actually, bypass (i.e., back-flow to the section above the upper packer) was measured in the field, which confirms that, albeit simple, model I captures the main physical phenomena. Figure 7 displays the temporal evolution of generated overpressure at the borehole and, superimposed, the temporal evolution of manually calibrated fracture permeability. As observed, the initial permeability renders a good fit until t=1.5h, moment at which the jacking pressure is achieved and the initial tight fracture is open, which leads to (1) the first sudden pressure drop under constant flow rate, and (2) the corresponding sudden permeability increase. A second pressure drop under constant flow rate occurs, e.g., at t=1.75h, with corresponding permeability increase. Notably, the proper fit of the shut-in episode at t=2h requires a sudden drop of fracture permeability. This effect is not observed at t=2.5 and 3.6h, when subsequent shut-in episodes took place.

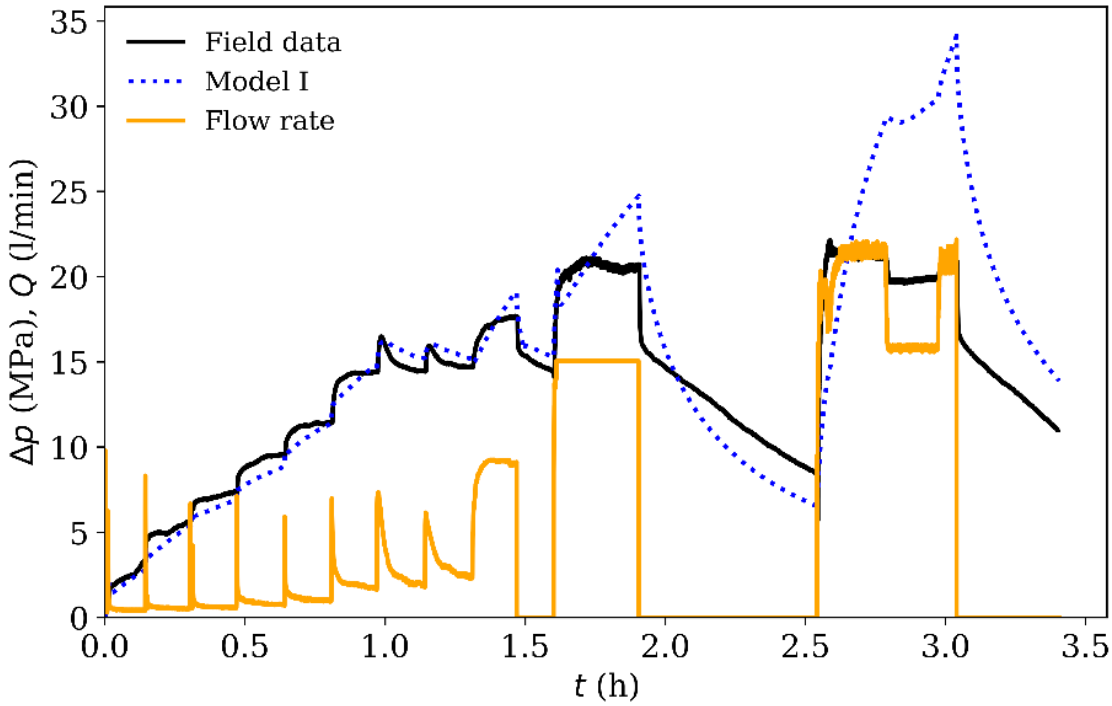

Figure 4. Calculated and measured pressure evolution at the injection well for the model with prescribed permeability (Model I). The injection scheme is also included for visualization purposes.

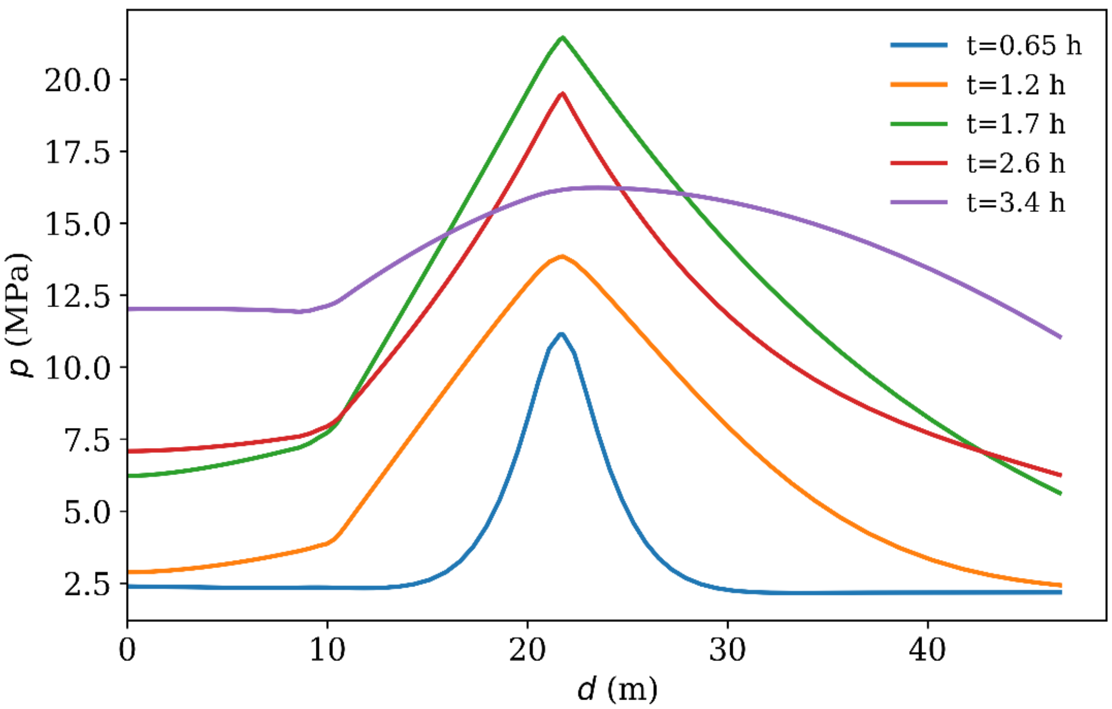

Figure 5. Pressure profile along the stimulated fracture at five times for Model I (see fracture profile in Figure 2). The borehole corresponds to d = 22 m., distance at which pressure peaks are obviously more prominent.

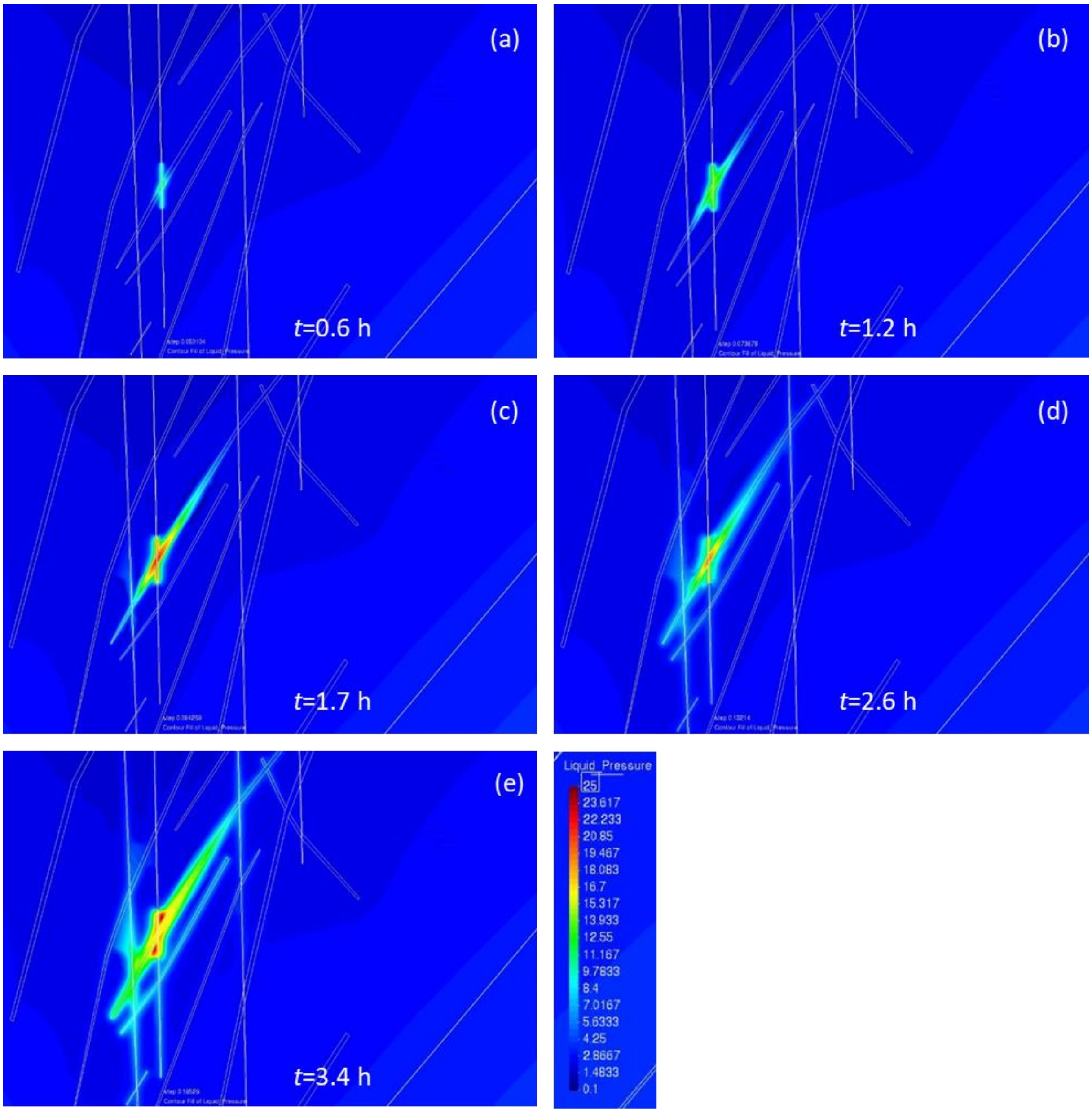

Figure 6. Contour plots of pore pressure (in MPa) at (a) 0.6 h, (b) 1.2 h, (c) 1.7 h, (d) 2.6 h and (e) 3.4 h after the start of stimulation for Model I.

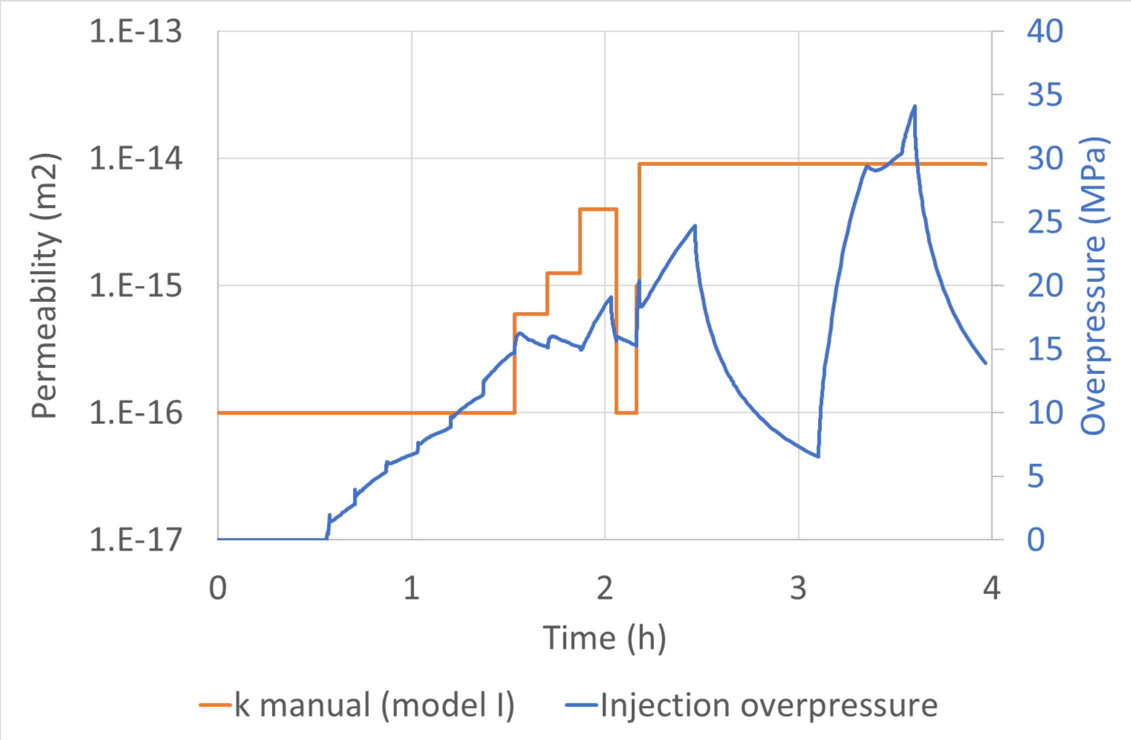

Figure 7. Temporal evolution of overpressure at the injection borehole and of manually calibrated fracture permeability.

3.2 Model II with variable permeability and elastic behaviour

The embedded model (Eq. (9)) accounts for both the spatial and temporal evolutions of fracture permeability. The green curve in Figure 8 depicts the temporal evolution of generated overpressure at the injection borehole predicted by the model with variable permeability as a function of fracture aperture (Model II). This model can accurately reproduce the field test results until 0.6 h. The subsequent discrepancy is likely due to dilatancy of the fracture and consequent permeability enhancement as the fracture reaches its yield point and undergoes shear slip. However, material behaviour is elastic in this model and thus, cannot reflect the proper mechanical response. Consequently, the generated strain is lower than the actual one, and the embedded model yields less permeability enhancement than the actual one. As a result, the calculated overpressure is higher than the field response due to the lower permeability.

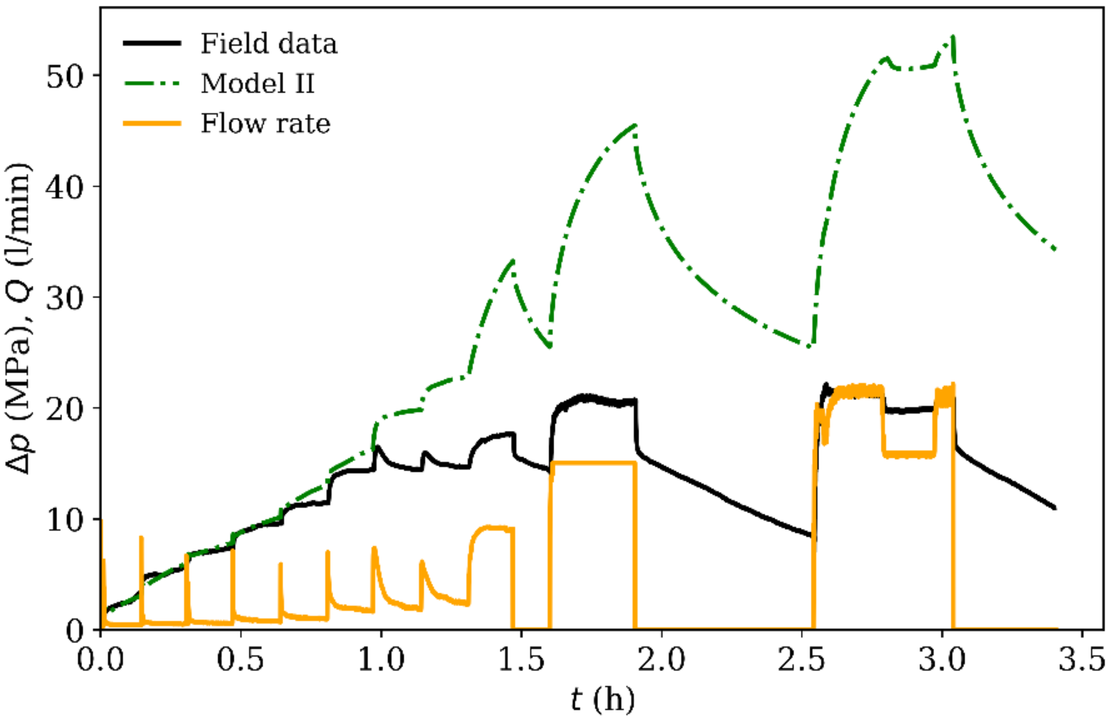

Figure 8. Temporal evolution of overpressure at the injection well for the model with variable permeability and elastic behaviour for the fracture (Model II).

The main issue with the model I is that fracture permeability is homogeneous at any given time. Using an embedded model (which is a function of volumetric strain, Figure 9) shows that permeability increases locally near the injection well and that enhancement is lower away from the well. The longitudinal profile of fracture permeability displays an increase (around 3 orders of magnitude at maximum) in fracture permeability due to the fracture aperture enhancement (Figure 10). Note that permeability enhancement occurs within the pressurized region of the fracture (Figure 11). As a result, the pore pressure perturbation of nearby fractures and wellbore occurs at a later stage and with lower magnitude as compared to Model I (Figure 12).

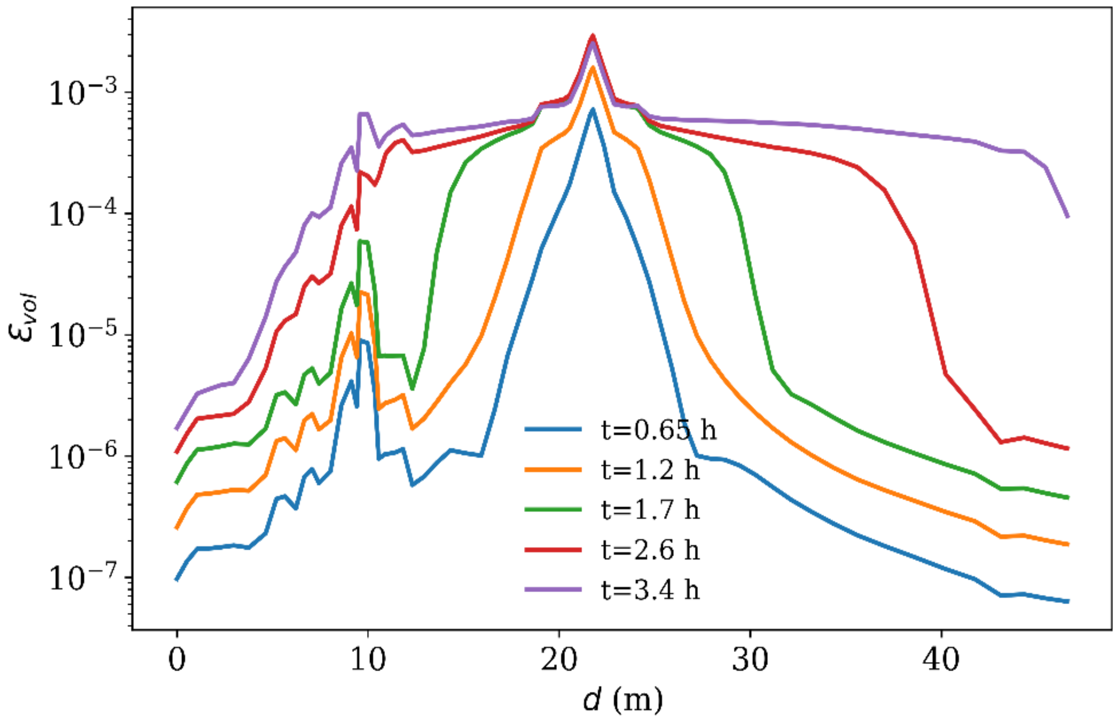

325

326 *Figure 9. Volumetric strain profile along the fracture with Model II (see fracture profile in Figure 2).*

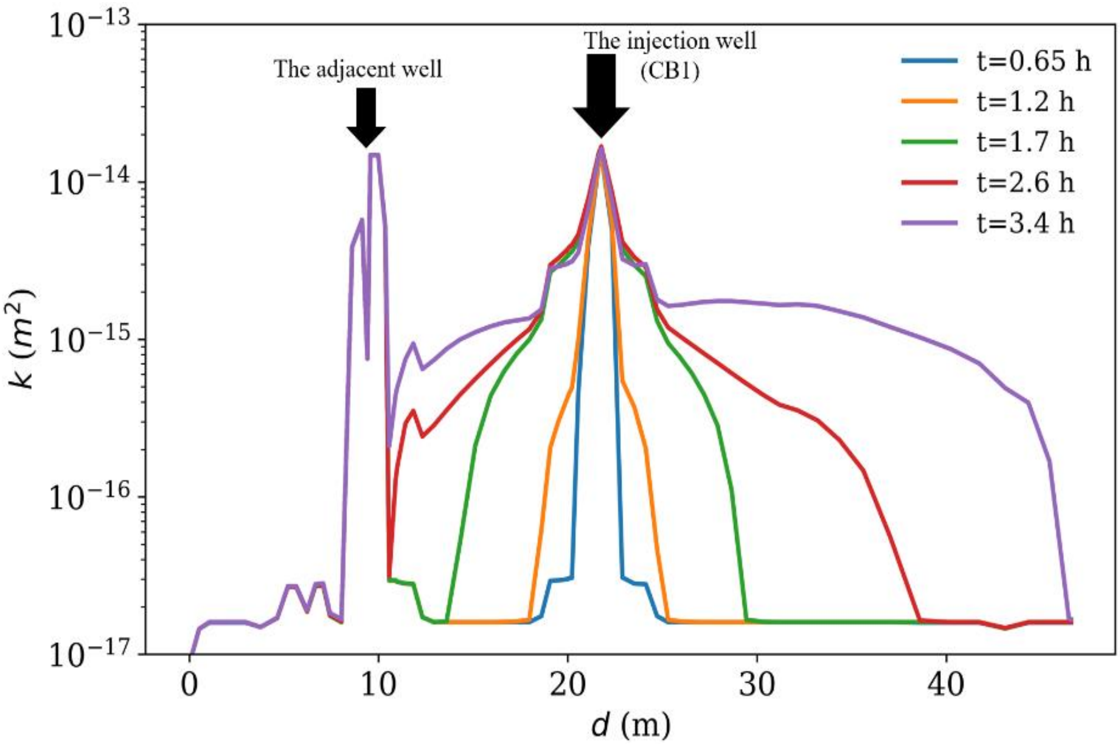

327

328 *Figure 10. Fracture permeability profile for five selected times during injection in Model II (see fracture*
329 *profile in Figure 2).*

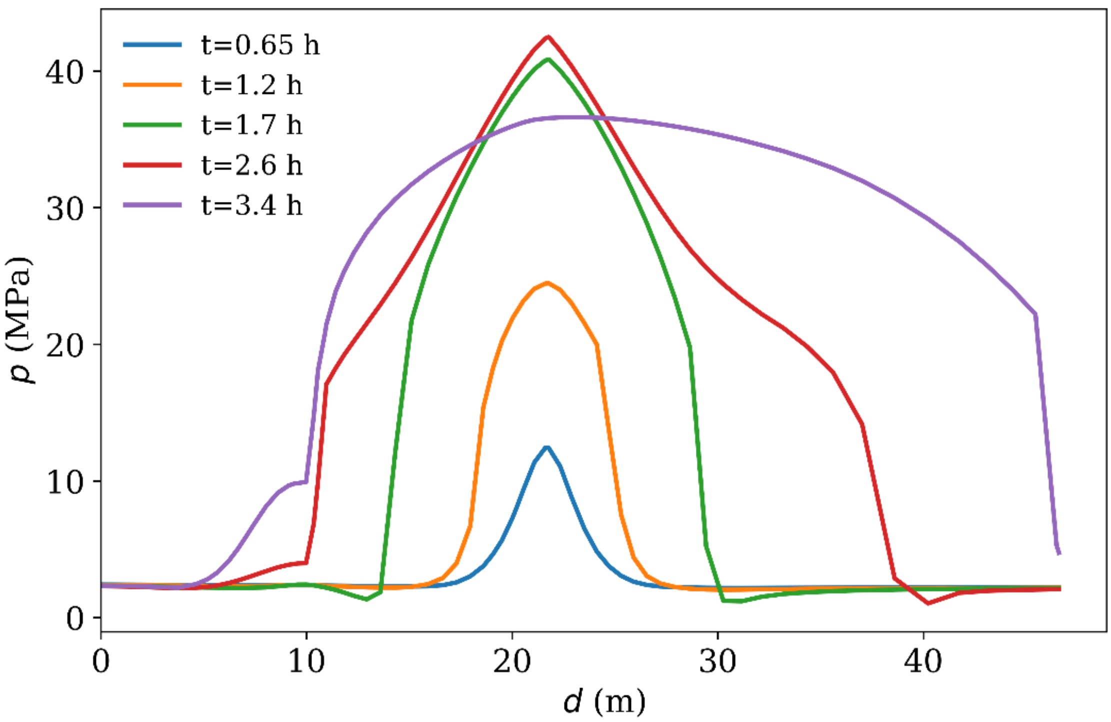

Figure 11. Pressure profile along the stimulated fracture at five times for Model II (see fracture profile in Figure 2).

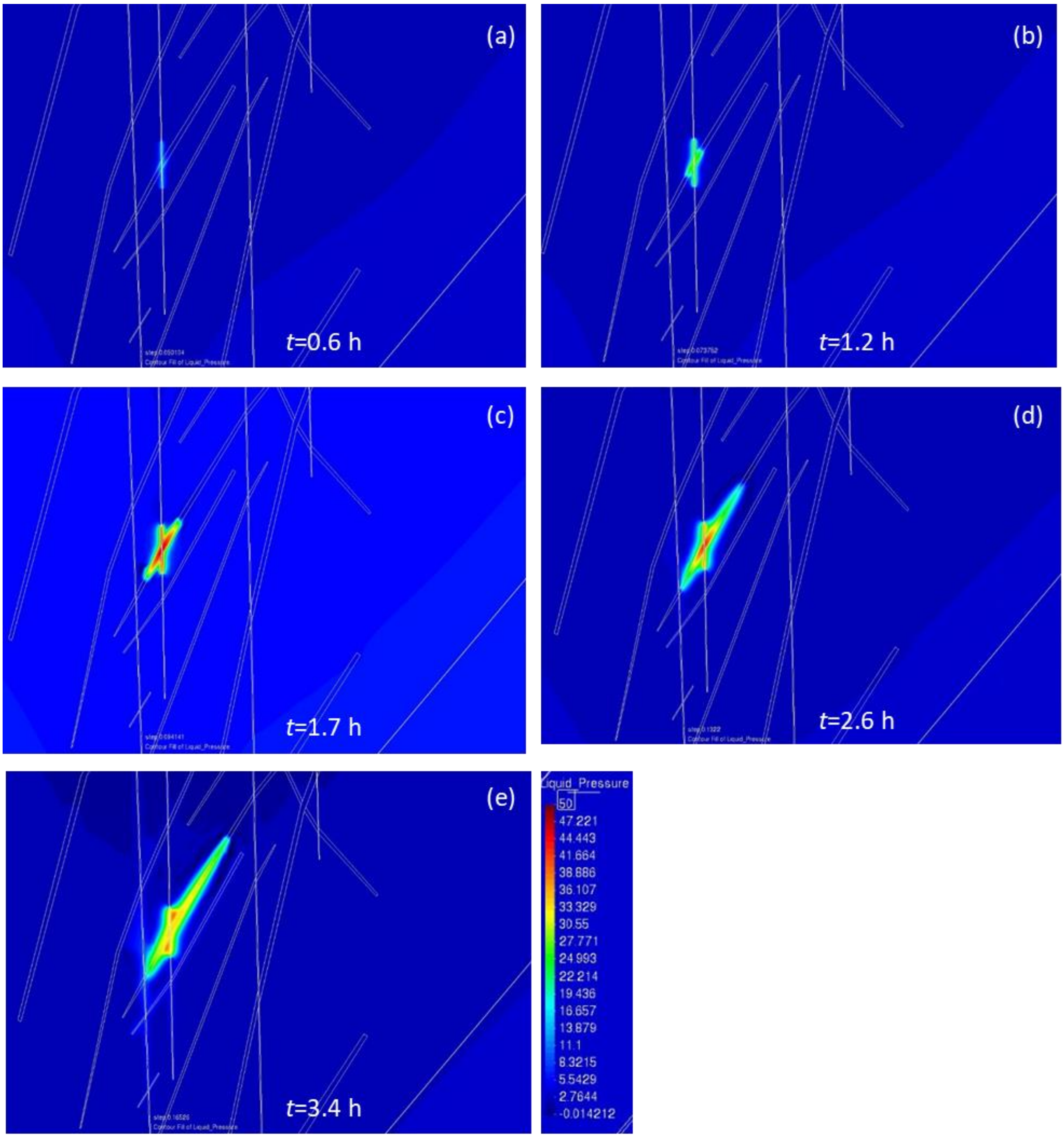

Figure 12. Contour plots of pore pressure (in MPa) at (a) 0.6 h, (b) 1.2 h, (c) 1.7 h, (d) 2.6 h and (e) 3.4 h after the start of stimulation for Model II

Figure 13 and Figure 14 display the contour plots of permeability and volumetric strain, respectively, at five selected control times. The pressurization of the fracture (Figure 12) causes its expansion (Figure 14), enhancing permeability (Figure 13). The permeability enhancement is moderate, with *k* remaining below 10^{-14} m^2, and thus, the predicted pressure build-up becomes excessively high compared to field measurements at late times.

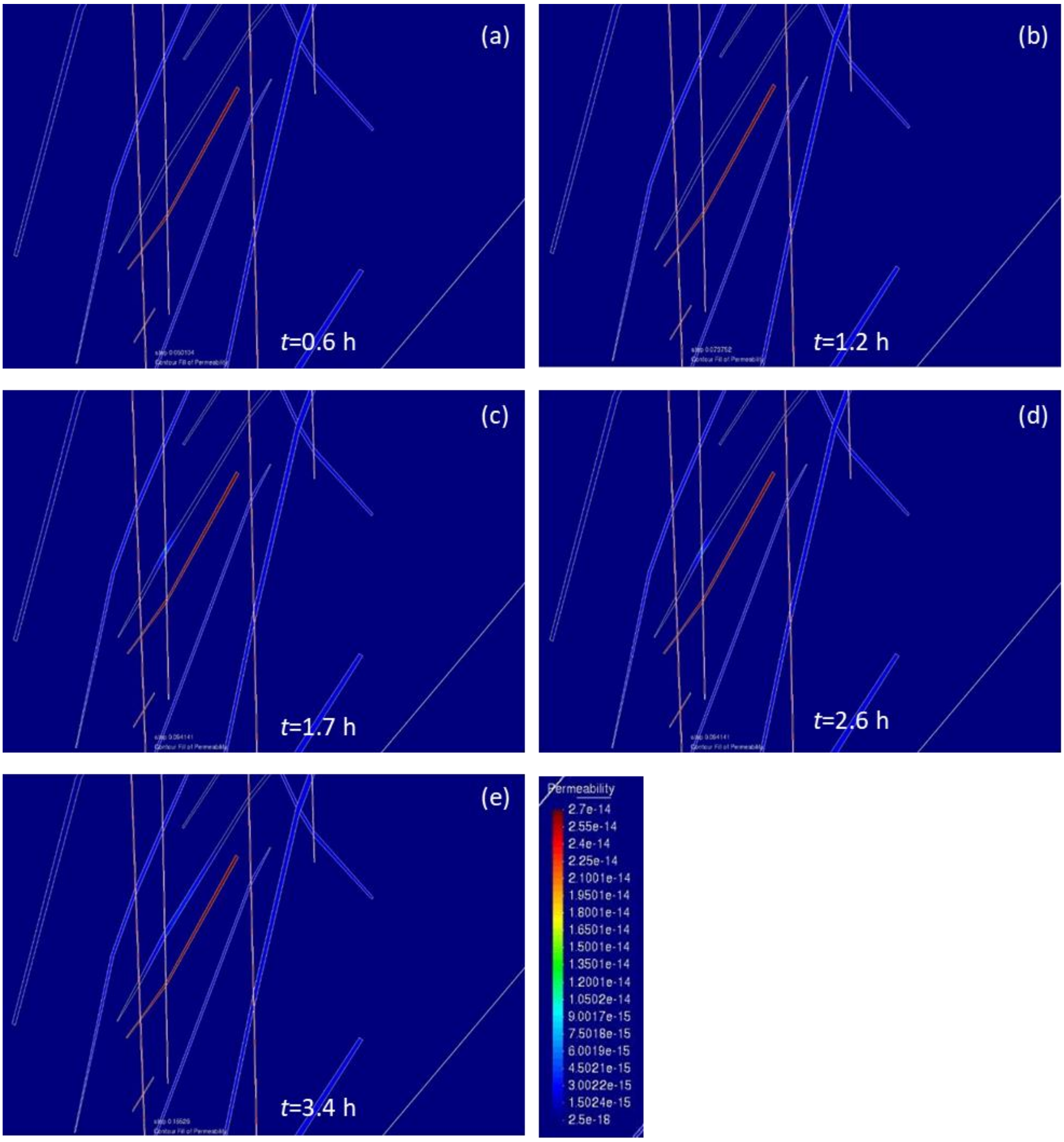

Figure 13. Contour plots of permeability (in m^2) at (a) 0.6 h, (b) 1.2 h, (c) 1.7 h, (d) 2.6 h and (e) 3.4 h after the start of stimulation for Model II.

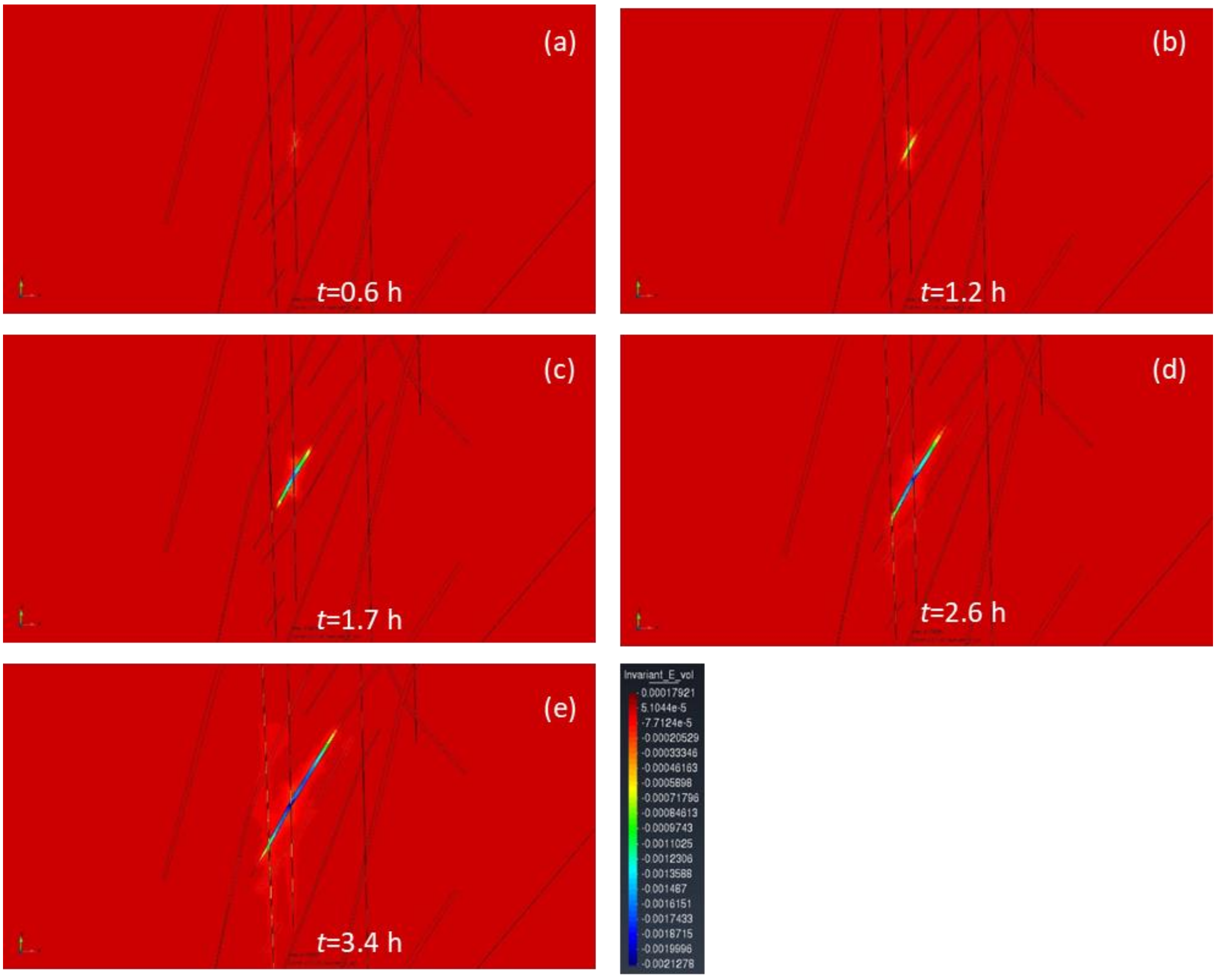

Figure 14. Contour plots of volumetric strain at (a) 0.6 h, (b) 1.2 h, (c) 1.7 h, (d) 2.6 h and (e) 3.4 h after the start of stimulation for Model II. Negative values (blue colours) indicate expansion.

3.3 Models III & IV with variable permeability and viscoplastic behaviour

To overcome the limitations of the elastic model in simulating the hydro-mechanical behaviour of the fracture after its reactivation, we utilize viscoplasticity with dilatancy and strength softening (equations 4-8). Note that models III and IV utilize the same constitutive equations but with slightly different parameters (Table 1). The remaining two models reproduce the temporal evolution of generated injection overpressure of the field test better than previous models, especially during the last injection phase (Figure 15).

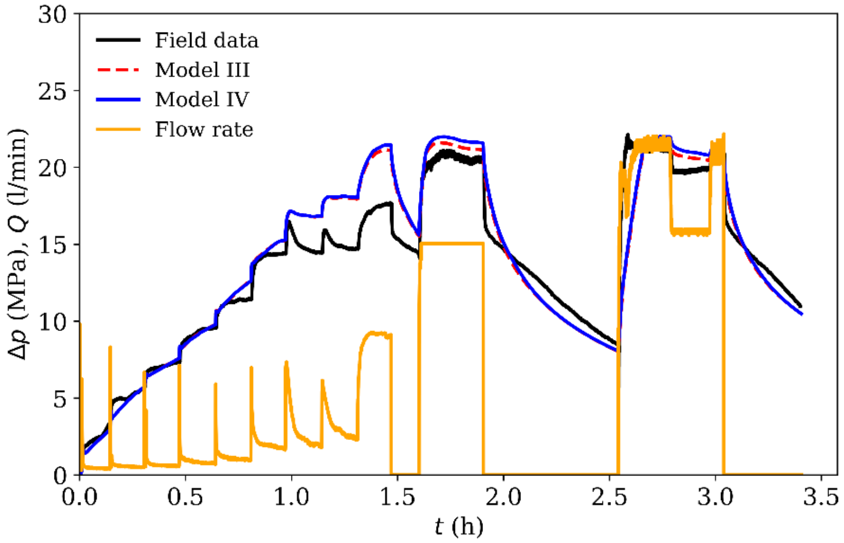

Figure 15. Temporal evolution of overpressure at the injection well using models with variable permeability and viscoplastic behaviour for the fracture (models III and IV).

These models allow to simulate fracture reactivation and yield an additional permeability enhancement (Figure 16 and Figure 17 for models III and IV, respectively) when compared with the elastic model (Figure 10). In this case, permeability enhancement is given by both elastic strain (Figure 18 and Figure 19 for models III and IV, respectively) and plastic strain (Figure 20 and Figure 21 for deviatoric and volumetric strain, respectively). Plastic strain further enhances fracture permeability, which smaller pressure build-ups and thus, to a better approximation of the field data (Figure 15).

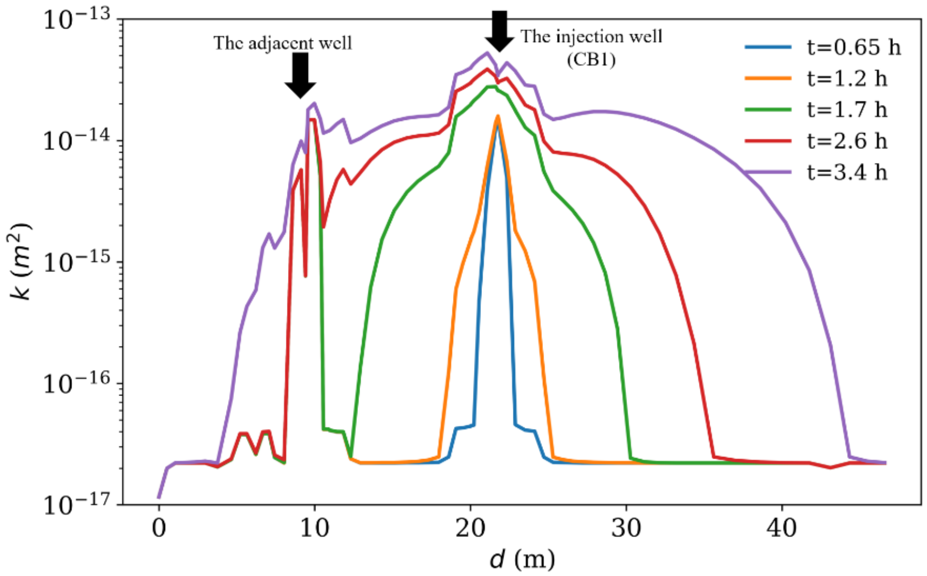

Figure 16. Longitudinal profile of fracture permeability at five selected times for Model III (see fracture profile in Figure 2).

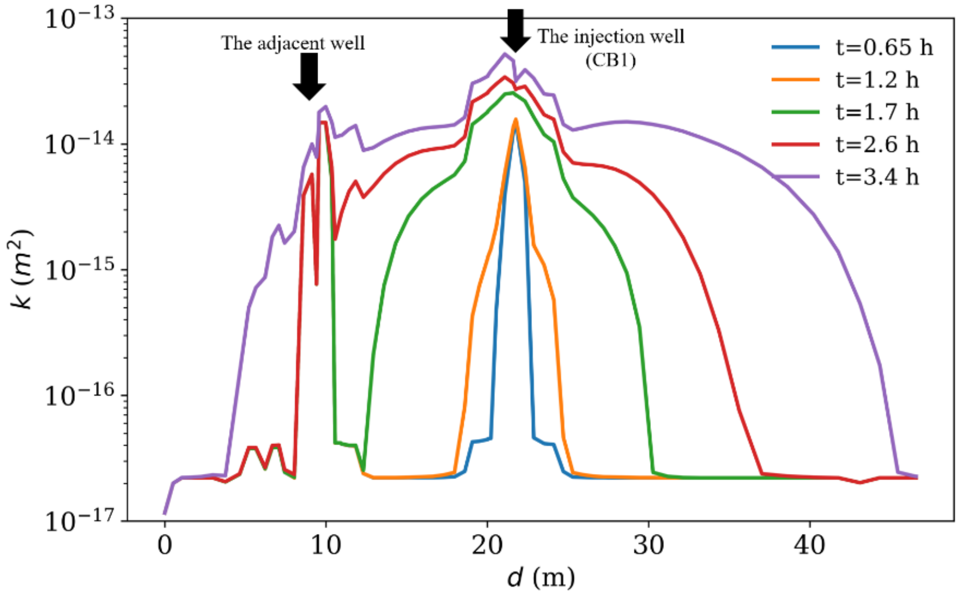

Figure 17. Longitudinal profile of fracture permeability at five selected times for Model IV (see fracture profile in Figure 2).

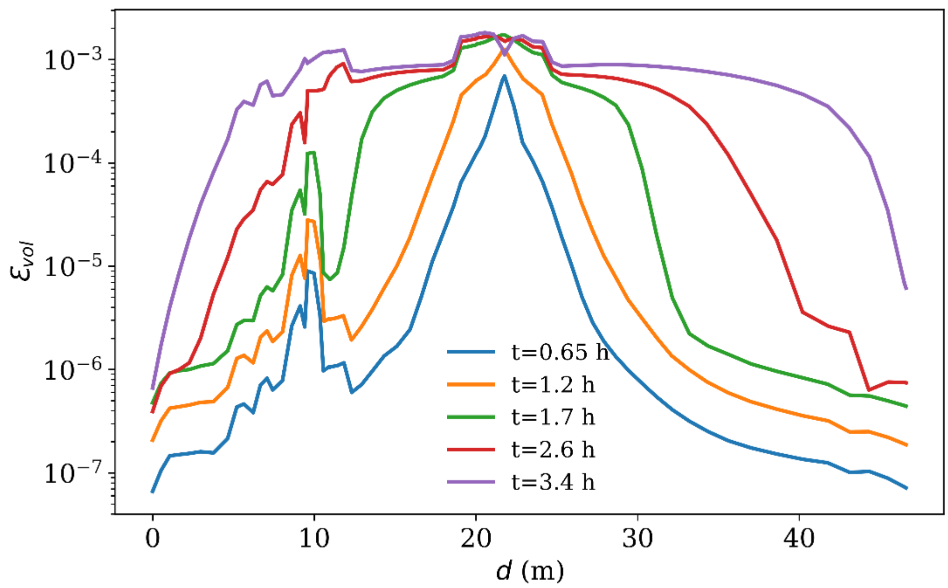

Figure 18. Volumetric strain profile along the fracture at five times for Model III (see fracture profile in Figure 2).

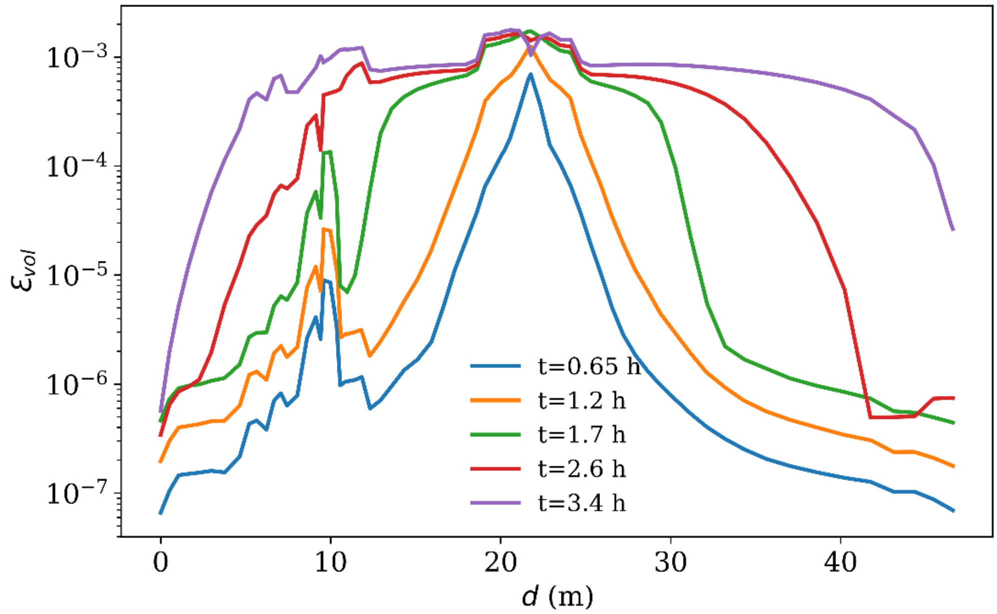

376

377 *Figure 19. Volumetric strain profile along the fracture at five times for Model IV (see fracture profile in*
378 *Figure 2).*

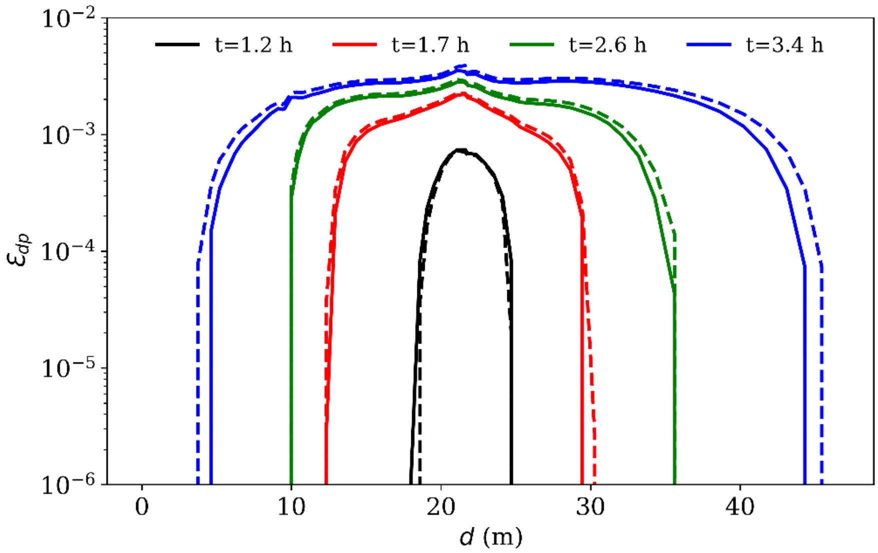

379

380 *Figure 20. The longitudinal profile of the deviatoric plastic strain at four times for both viscoplastic*
381 *models (solid lines: Model III, hyphened lines: Model IV) (see fracture profile in Figure 2).*

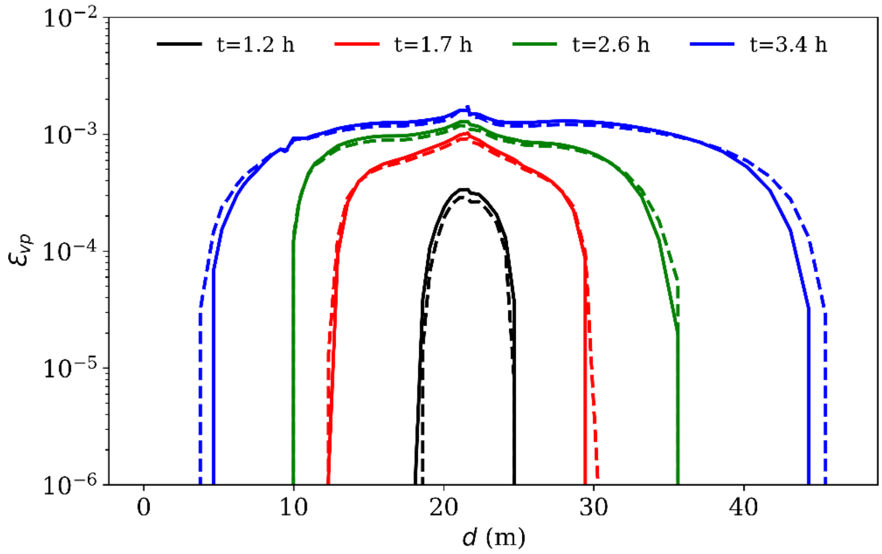

Figure 21. The longitudinal profile of the volumetric plastic strain at certain times for both viscoplastic models (solid lines: model III, hyphened lines: model IV) (see fracture profile in Figure 2).

The pore pressure build-up along the stimulated fracture (Figure 22 and Figure 23 for models III and IV, respectively) mainly occurs within the reactivated region with irreversible strain (recall Figure 20 and Figure 21). For illustrative purposes, we show the contour plots of pore pressure (Figure 24), permeability (Figure 25), volumetric strain (Figure 26) and deviatoric plastic strain (Figure 27) for Model III. The results for Model IV are very similar to those of Model III. Note that as the stimulation progresses, pressure diffusion advances across the intact rock matrix and affects nearby fractures. Furthermore, ahead of the pressurization front, extension occurs in certain zones of the rock matrix, causing pressure drop. When accounting for fracture reactivation and dilatancy, the fracture opens significantly as a result of shear slip, causing a permeability enhancement of several orders of magnitude that significantly lowers pore pressure build-up.

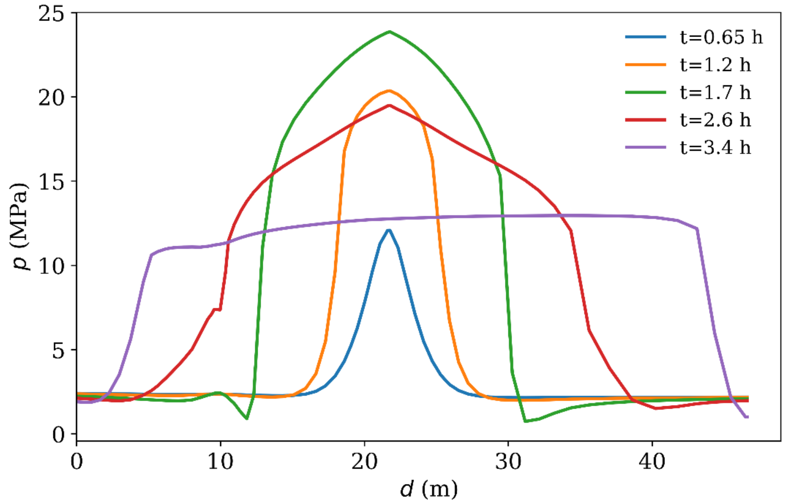

Figure 22. Pressure profile along the stimulated fracture at five times for Model III (see fracture profile in Figure 2).

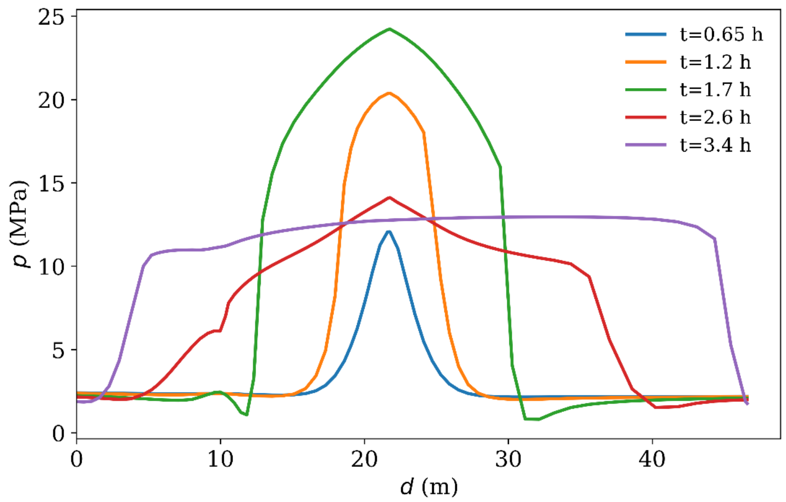

Figure 23. Pressure profile along the stimulated fracture at five times for Model IV (see fracture profile in Figure 2).

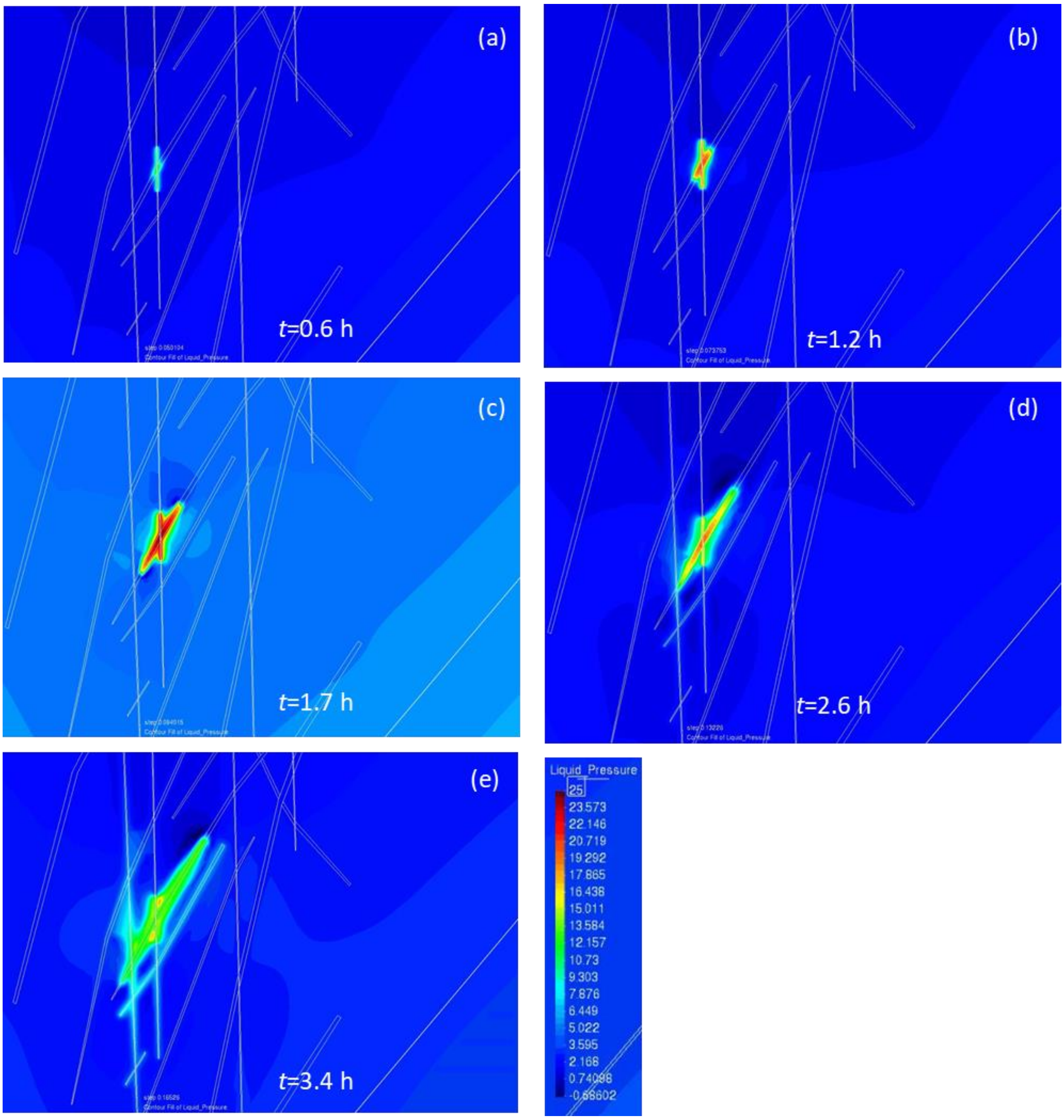

Figure 24. Contour plots of pore pressure (in MPa) at (a) 0.6 h, (b) 1.2 h, (c) 1.7 h, (d) 2.6 h and (e) 3.4 h after the start of stimulation for Model III.

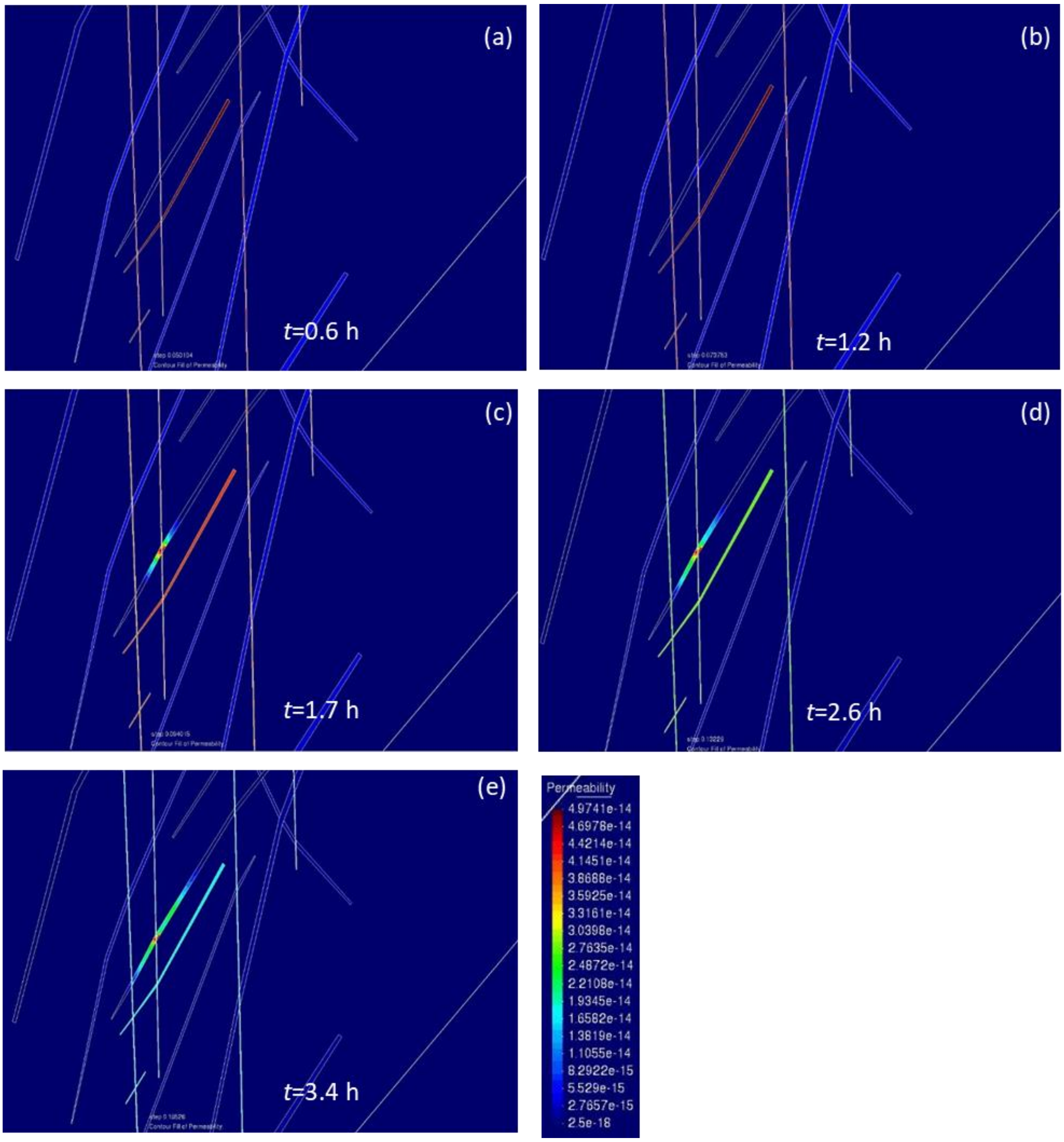

Figure 25. Contour plots of permeability (in m^2) at (a) 0.6 h, (b) 1.2 h, (c) 1.7 h, (d) 2.6 h and (e) 3.4 h after the start of stimulation for Model III.

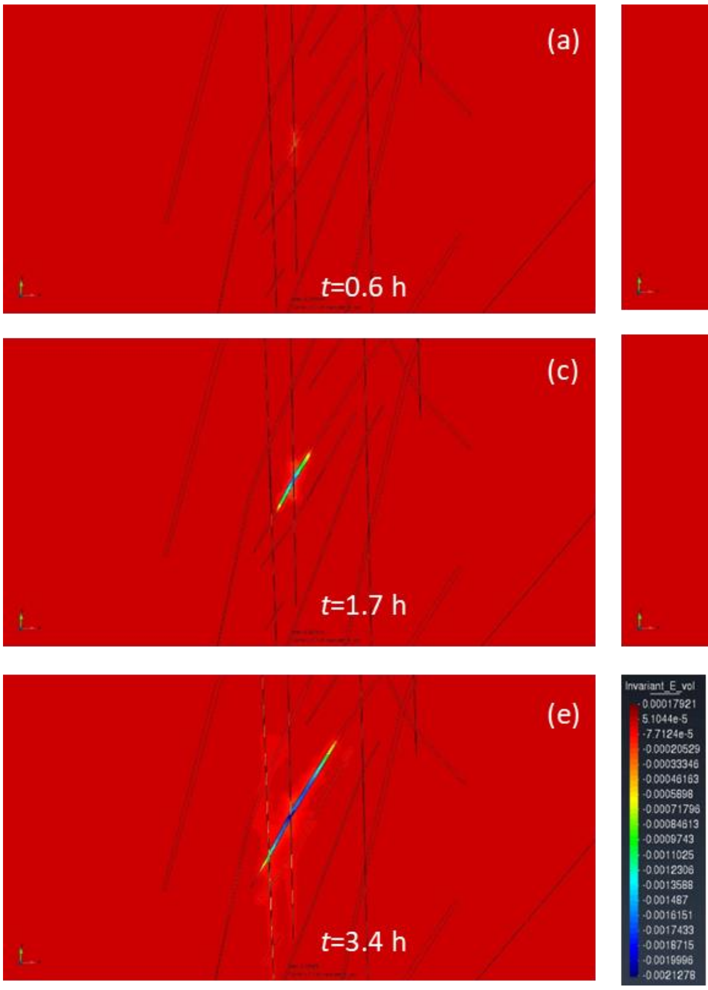

Figure 26. Contour plots of volumetric strain at (a) 0.6 h, (b) 1.2 h, (c) 1.7 h, (d) 2.6 h and (e) 3.4 h after the start of stimulation for Model III.

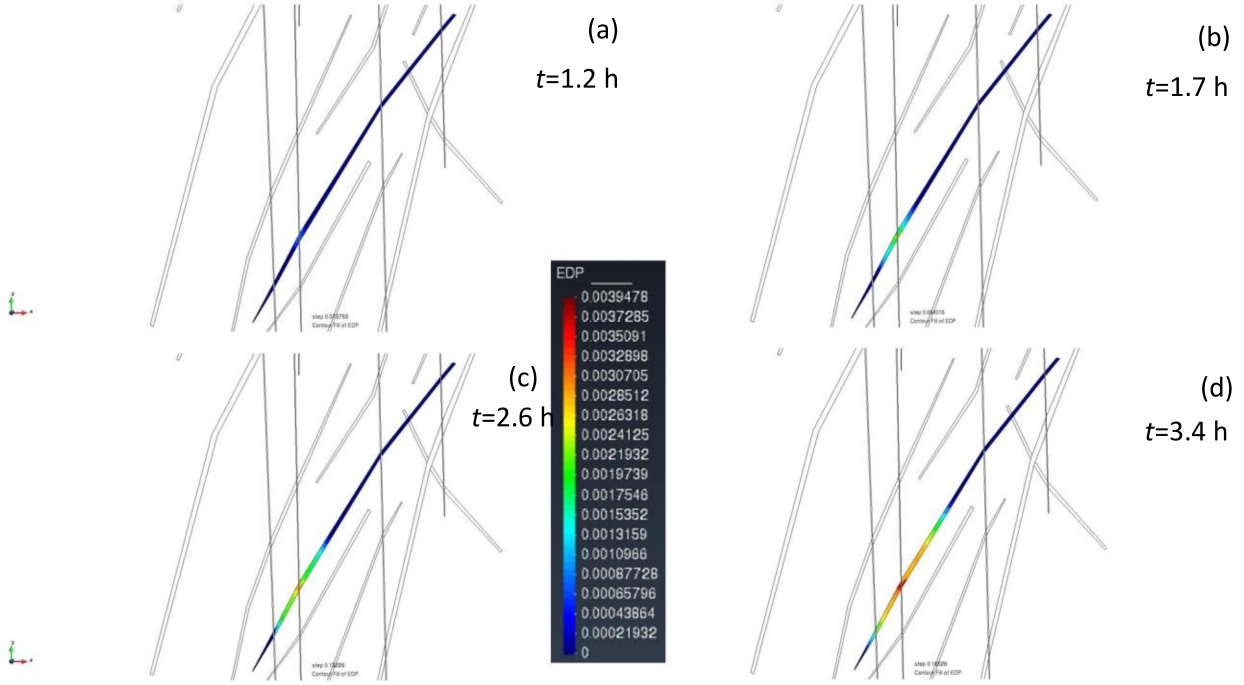

Figure 27. Contour plots of deviatoric plastic strain at (a) 1.2 h, (b) 1.7 h, (c) 2.6 h and (d) 3.4 h after the start of stimulation for Model III. Note that at 0.6 h, the fracture has not failed yet.

We choose three points in the fracture to monitor the evolution of the deviatoric plastic strain during injection (Figure 28). The strain sharply rises after failure in the three points. Once failure occurs, the plastic strain increases sharply and, later on, plastic strain accumulates at very low rate. The reactivation front, which coincides with the sharp increase in plastic strain, progressively advances away from the injection well (Figure 21), advancing not far behind the pressurized region, as indicated by the region with elastic volumetric strain (Figure 18 and Figure 19). Plastic strain propagates by the end of the simulation at 45 m of the fracture, i.e., some 20 m away from the injection well.

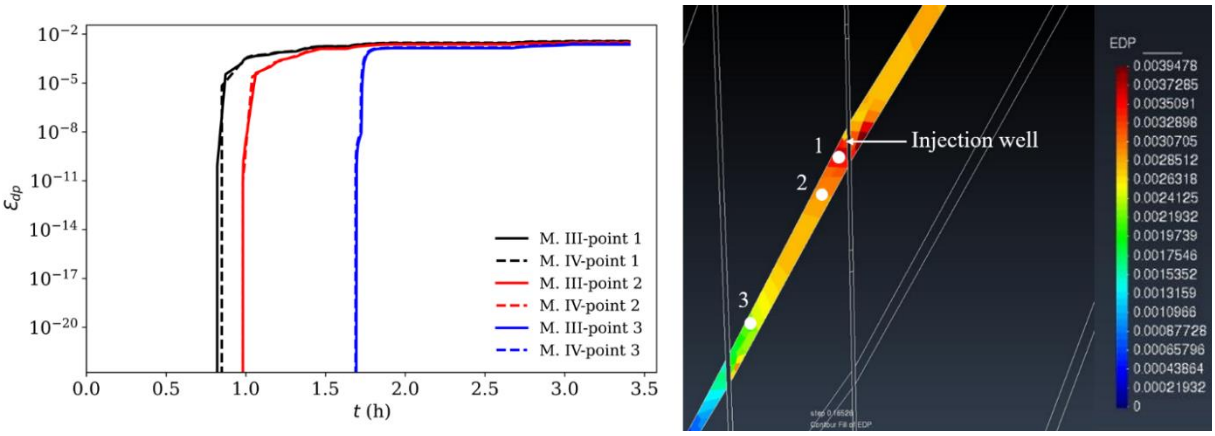

Figure 28. The evolution of the deviatoric plastic strain at three different point in the fracture. Point 3 is placed some 10 m away from the injection well.

Pressurization of the fracture causes a poromechanical response of the rock matrix, inducing shear stress that affects nearby fractures (Figure 29). Initially, the induced stresses are reversible (Figure 29a) and would vanish shortly after shut-in. However, once the fracture is reactivated, an irreversible stress drop occurs within the slipped zone and the loves of positive shear stress are displaced following the tips of the slipped zone (Figure 29b-e). As slip accumulates, the region with shear stress changes extends, affecting fractures that are placed further away from the stimulated fracture. Thus, stimulation of a single fracture modifies the stability of nearby fractures.

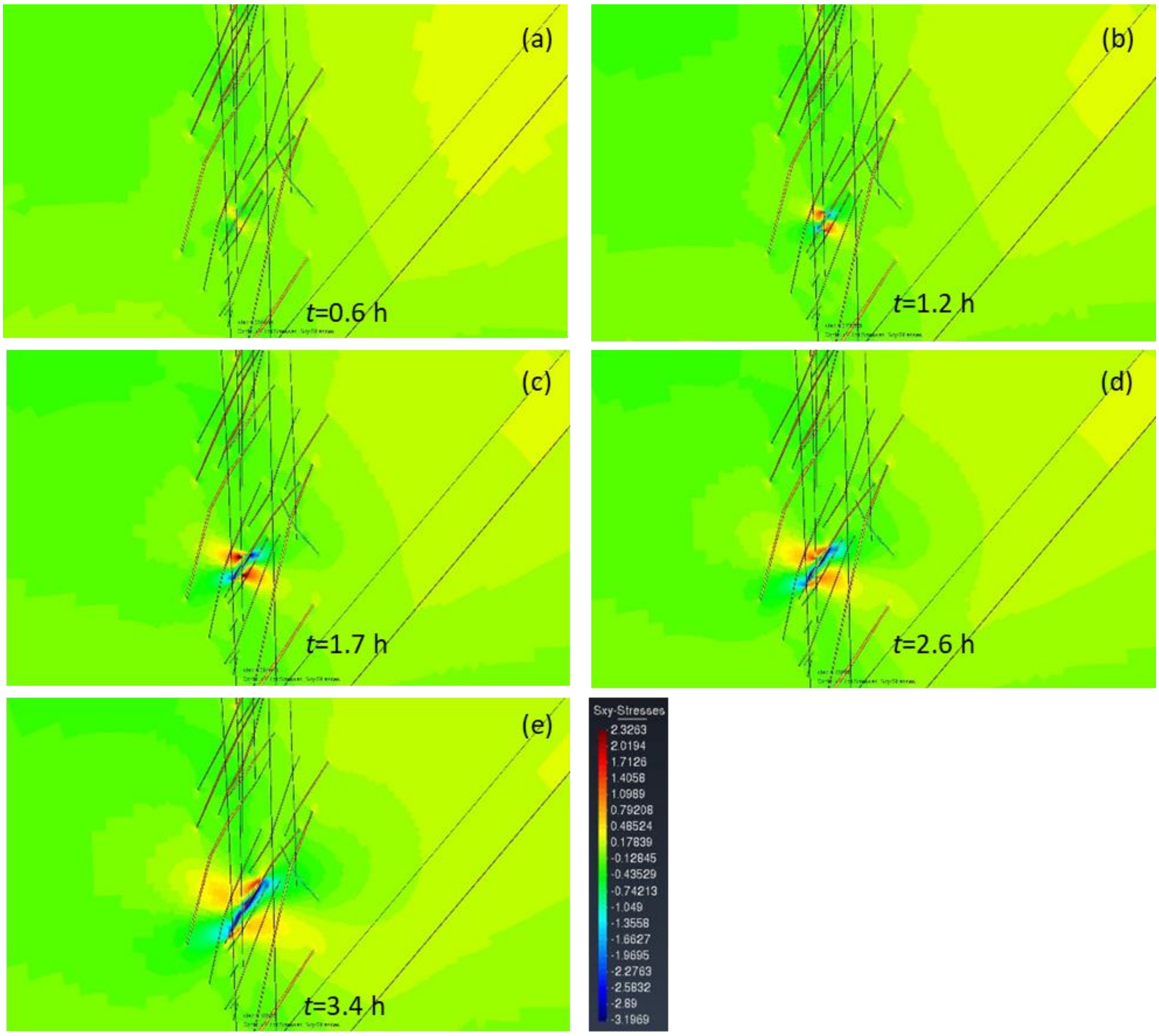

Figure 29. Contour plots of shear stress at (a) 0.6 h, (b) 1.2 h, (c) 1.7 h, (d) 2.6 h and (e) 3.4 h after the start of stimulation for Model III.

Figure 30 depicts the stress paths, which represent the successive states of stress during the stimulation test, at the three points shown in Figure 28. Figure 30 also shows the failure surfaces at the peak friction angle for both viscoplastic models (III and IV). The initial stress is always stable and is directed towards the failure surface as pore pressure increases, with constant or increasing deviatoric stress. The *q-p′* trajectories of Model IV do not display the slip weakening, which means that the critical value of the softening parameter should be smaller than the selected 0.001 to have a marked effect.

Note that the plastic strain is very similar in both models until late times of the test (Figure 20 and Figure 21). Failure occurs under compression in all cases.

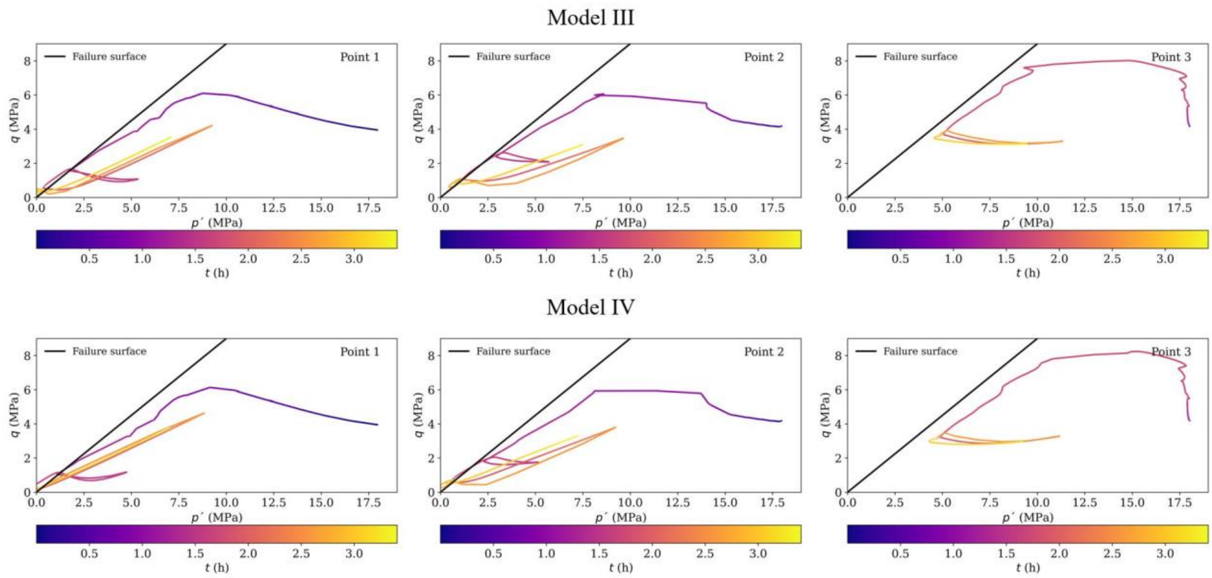

Figure 30. Effective stress path for both viscoplastic models and their failure surface for three different points located within the fracture (points are indicated in Figure 28).

We have continued the simulation of Model IV for three more injection cycles. The pore pressure evolution at the well reproduces fairly well the field measurements (Figure 31). Thus, our model reproduces the progressive hydraulic stimulation of the fracture, which enhances permeability away from the injection well as the number of injection cycles accumulates (Figure 32). Permeability enhancement occurs at 36 m away from the injection well in the fifth injection cycle in which microseismic events are induced (Figure 32). Field measurements display a sharper pressure response at the well, both at the onset of injection and after shut-in, which may indicate instantaneous opening and closing of the fracture that is not fully captured by the numerical model (Figure 31). A number of microseismic events could be located during the field experiment (dots in Figure 30). They coincide with the injection periods as the fracture undergoes shear slip as a result of pressurization.

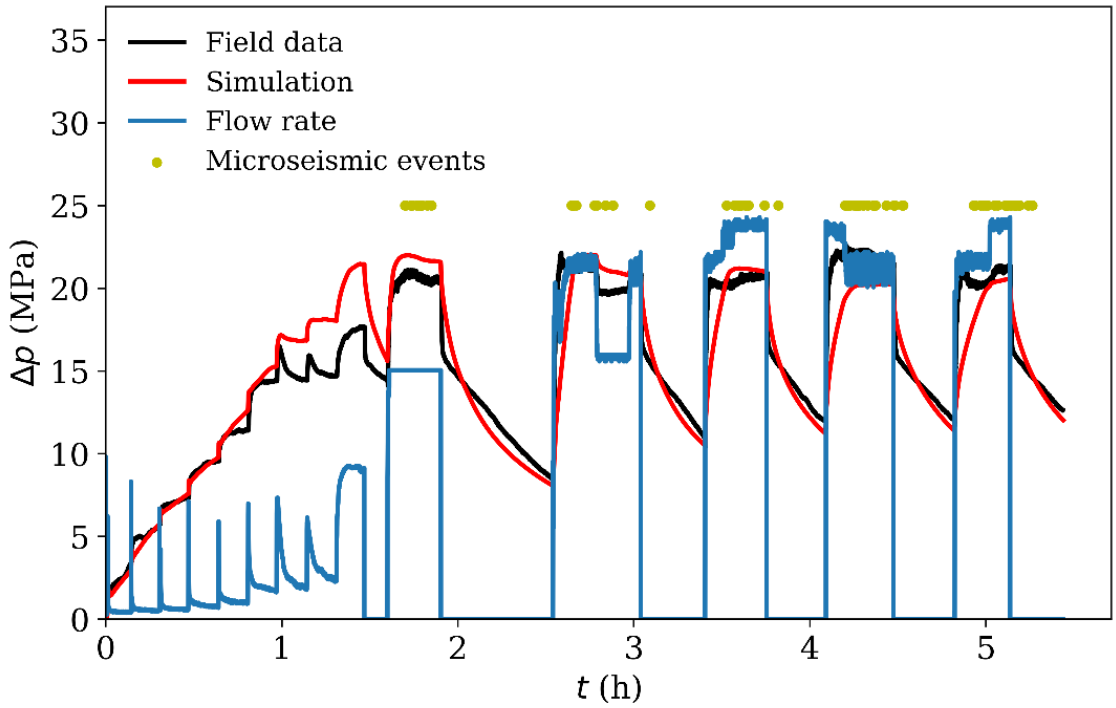

Figure 31. Pressure evolution and flow rate at the injection well for a larger number of injection cycles for Model IV compared to the field measurements. The time of occurrence of the microseismic events is indicated with a dot.

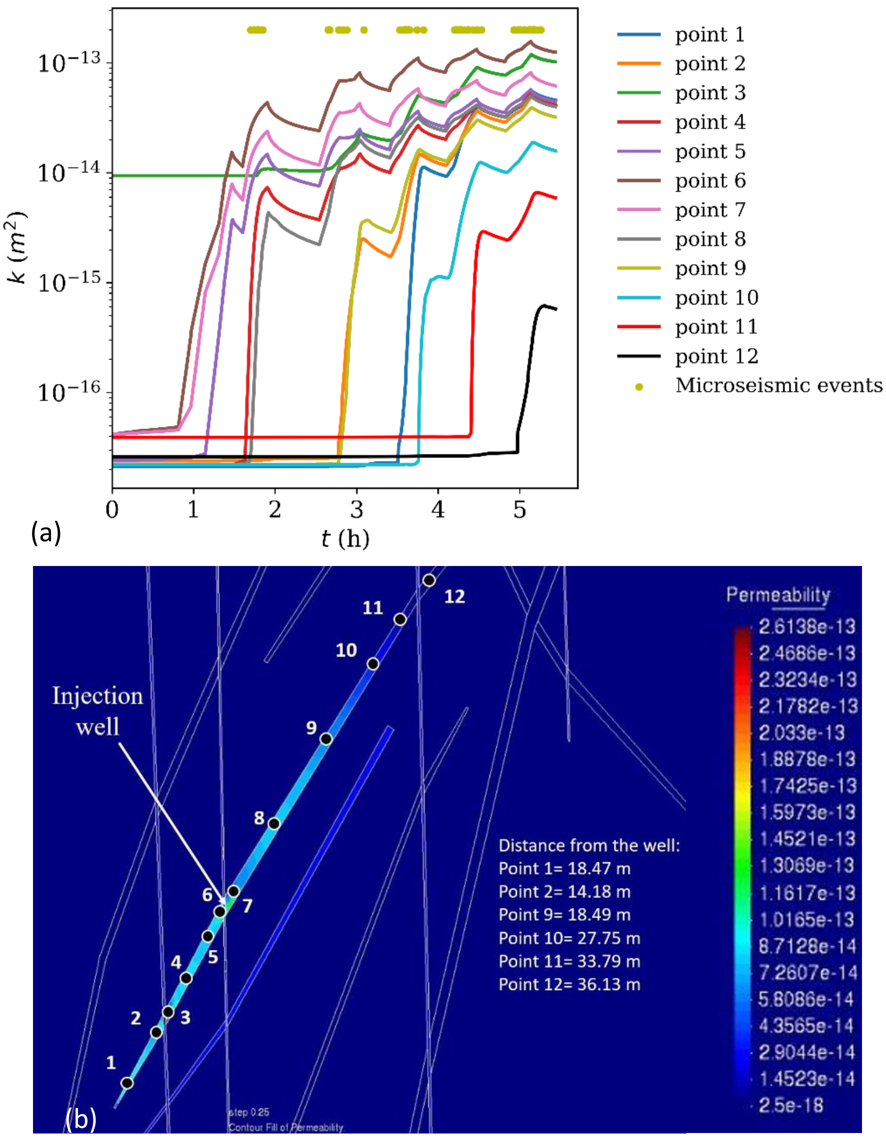

Figure 32. (a) Permeability evolution at several points along the fracture together with the time of occurrence of the microseismic events. The sharp permeability increase indicates when the pressure perturbation front reaches each point. (b) the location of each point along the fracture, with the permeability after 6 hours of stimulation in the background. The injection well is located in point 6 and as a reference, point 3 is located 12 m away from the injection well.

3.4 Comparison of all models

The comparison between pore pressure evolution calculated by models I to IV highlights that viscoplastic models better reproduce field test data. At the timestamp of microseismic events (yellow dots in Figure 33), models I and II forecast significantly larger overpressure compared to the measured one. Thus, according to models I and II, microseismic events after shear failure should have occurred way before. This discrepancy suggests that the fracture was undergoing progressive shear slip and opening due to dilatancy, and thus permeability enhancement, when the microseismic events were monitored.

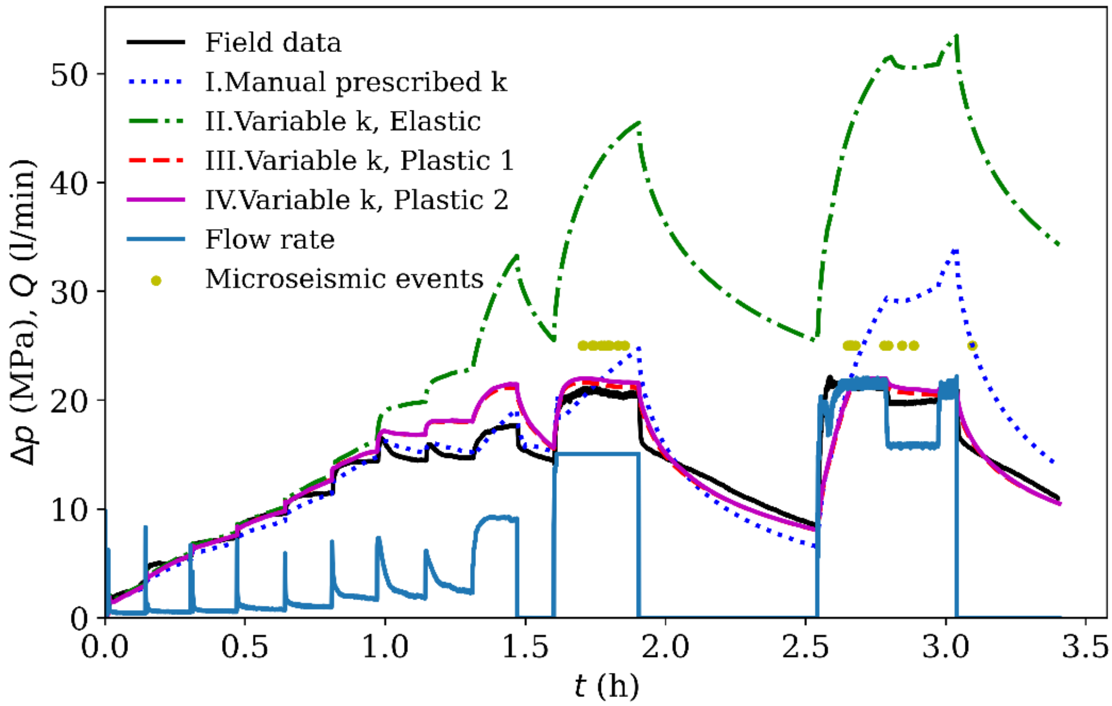

Figure 33. Pressure evolution at the injection well for the field experiment as well as the four numerical models; the solid blue line represents injection flow rate (lit/min); yellow dots indicate the time of the microseismical events.

Note that permeability enhancement is one order of magnitude larger for the viscoplastic models than for the elastic models (Figure 34). Albeit some permeability drops during shut-in periods (associated with partial fracture closure) are observed, the overall permeability enhancement is permanent and thus, contributes to improve borehole injectivity and eventually to connect a doublet. Note that the microseismic events correspond to moments of permeability enhancement. The sharp permeability enhancement in Point 3 (see Figure 28) that coincides with the first microseismic events could be associated with shear slip of the fracture around that point (Figure 31c).

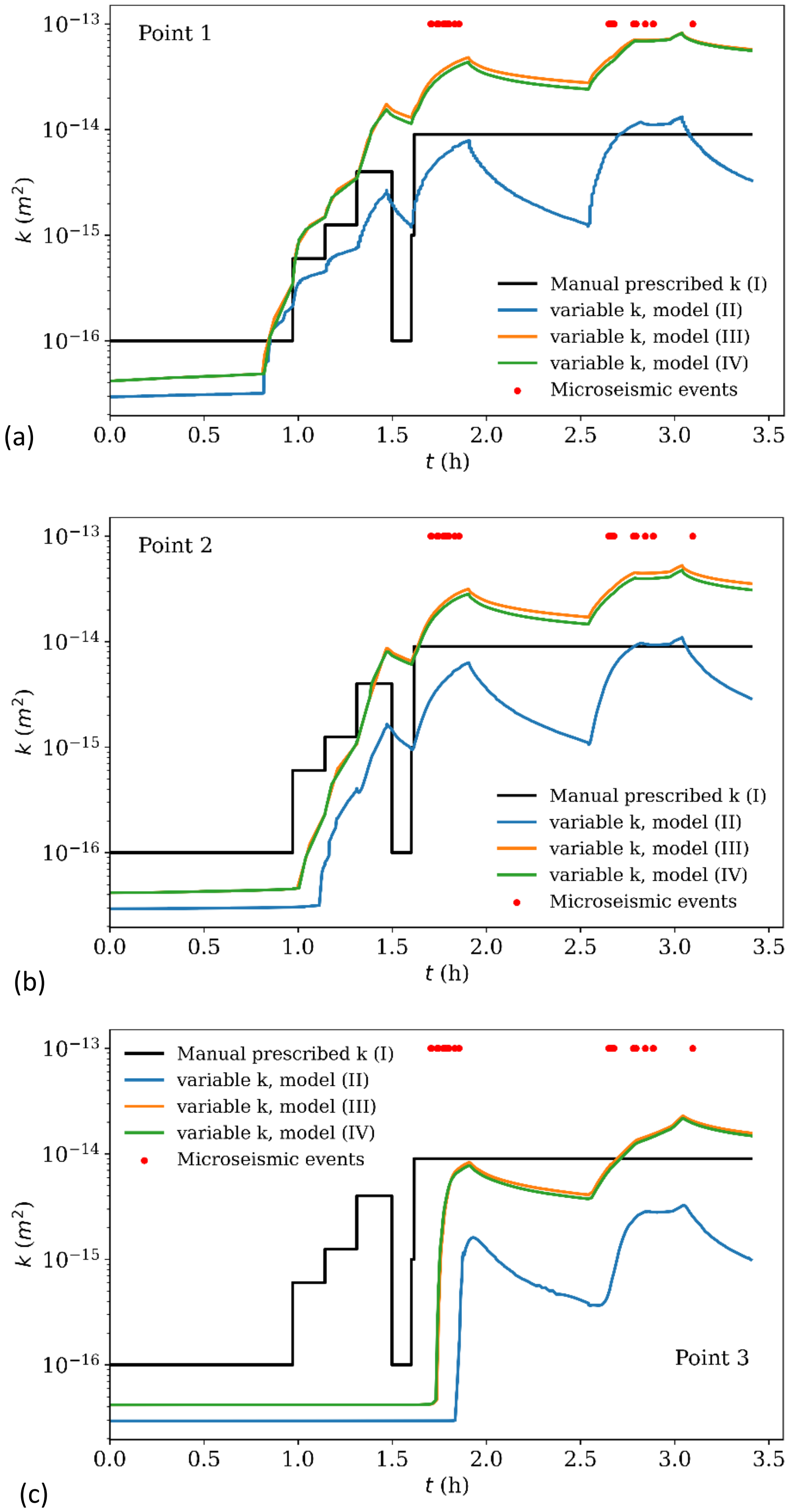

Figure 34. Fracture permeability evolution in models with prescribed and variable permeability at points (a) 1, (b) 2 and (c) 3 indicated in Figure 28.

The comparison between permeability profiles along the fracture indicates larger enhancement of permeability (Figure 35) due to the larger increase of fracture opening () in viscoplastic models. The permeability enhancement of one order of magnitude extends up to 40 m along the fracture towards the end of the stimulation. Both models III and IV yield similar results, which highlights the non-uniqueness of characterizing the strength of stimulated fractures by calibrating field data. Given that the pore pressure evolution predicted by the model fits well the one observed in the field, the stimulated area shown in the model gives an idea of which could be the actual one.

Figure 37 highlights the differences in pore pressure along the fracture for models I, II and III once the fracture is reactivated, i.e., for times longer than 0.65 h. Simulation results show that when the permeability is manually changed in the whole fracture (model I), pore pressure diffuses along the whole fracture, yielding a pore pressure distribution that differs from the actual one. When simulating variable permeability as a function of the injection-induced fracture aperture changes (models II and III), pore pressure diffusion occurs slowly because of the low initial fracture permeability. The region where pore pressure increases undergoes extension, and dilation in model III when shear failure conditions are reached, enhancing permeability. The effect of the additional permeability enhancement caused by shear slip is evident when comparing the pore pressure profiles of models II and III: pressure build-up is lower in the viscoplastic model than in the elastic one.

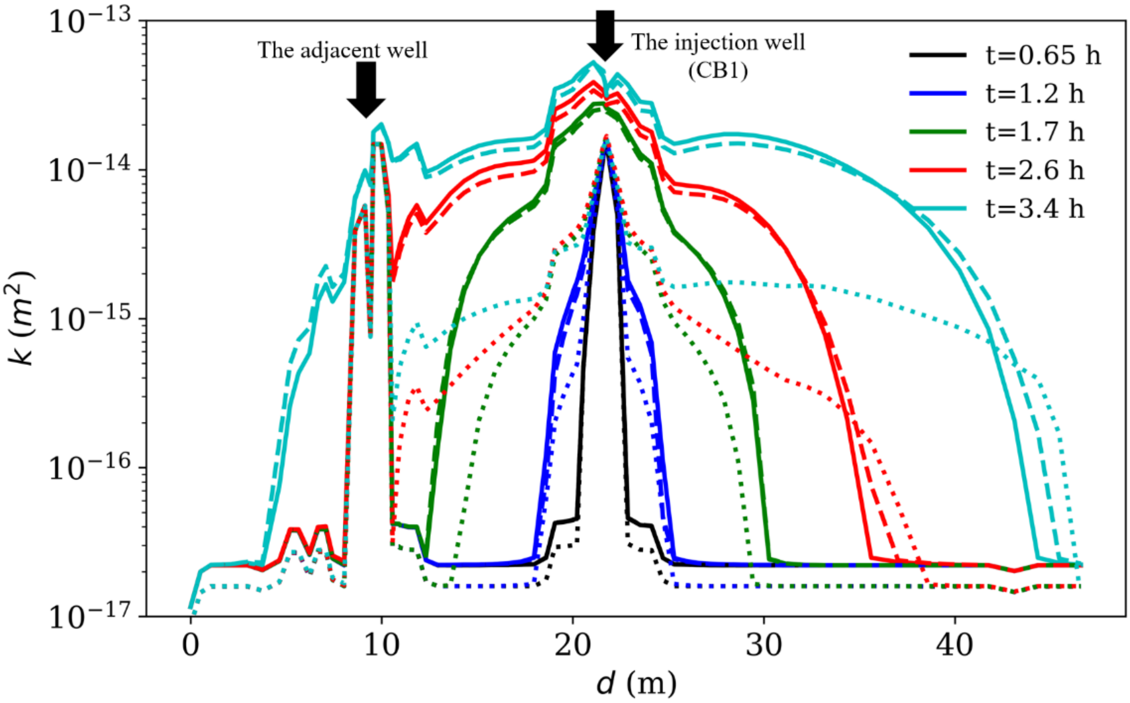

Figure 35. Comparison of fracture permeability profile for different models; solid lines represent viscoplastic Model III, hyphened-lines represent viscoplastic Model IV, and dotted-lines are for elastic Model II (see fracture profile in Figure 2).

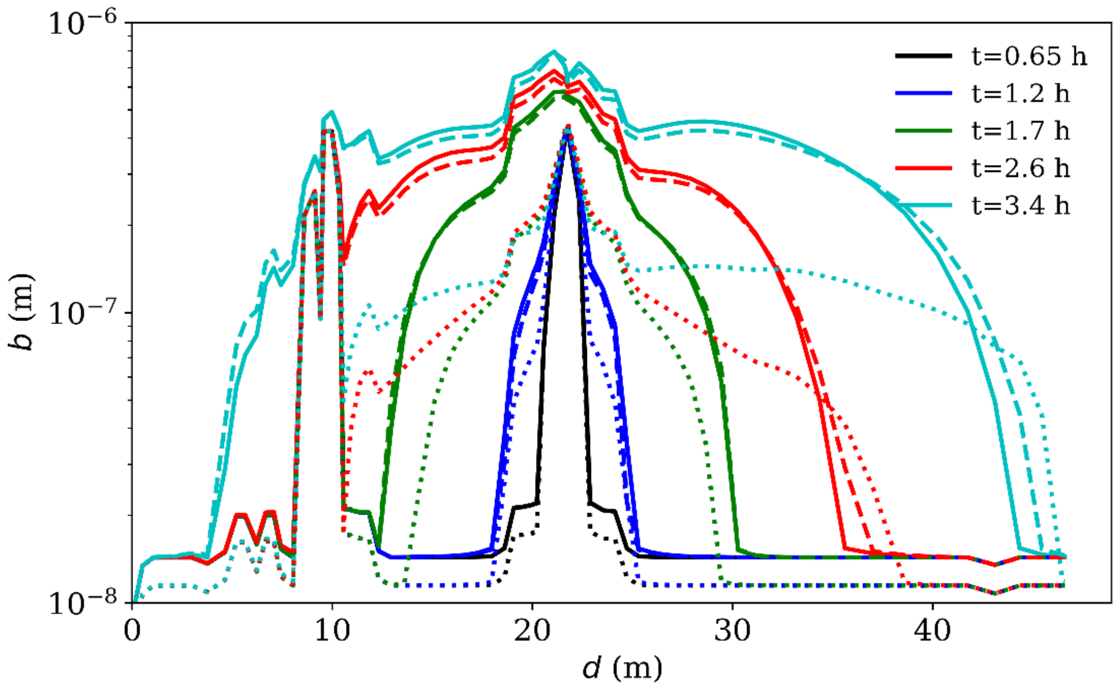

Figure 36. Comparison of fracture aperture along the stimulated fracture for the viscoplastic models III (solid lines) and IV (dashed lines), and the elastic model II (dotted lines) at five times of stimulation.

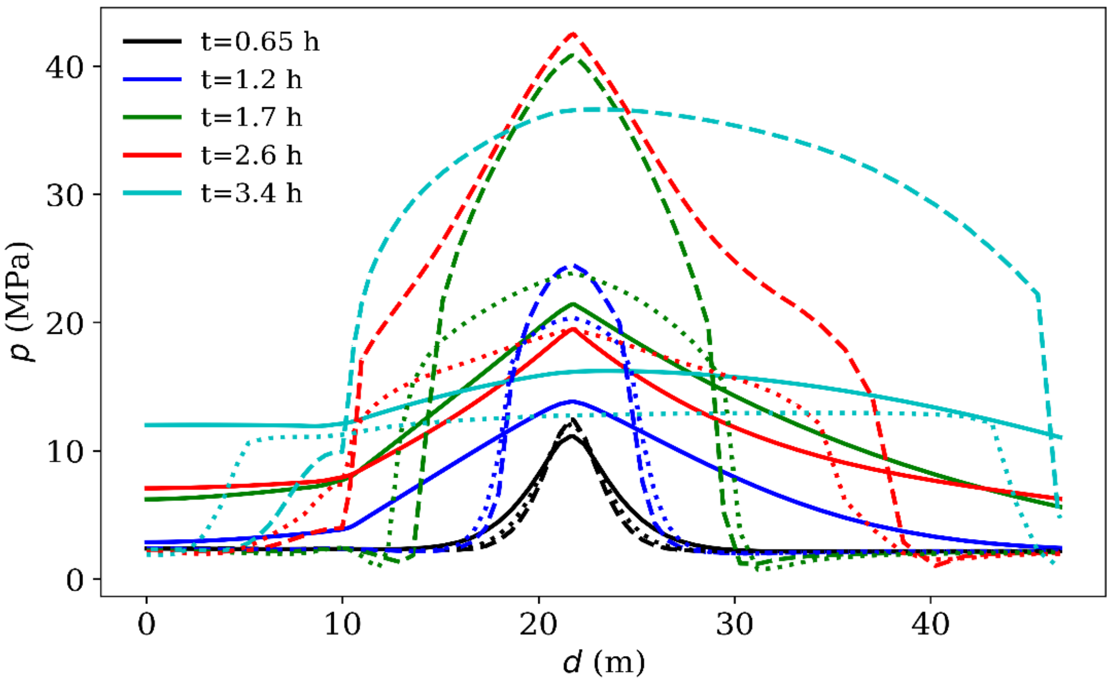

Figure 37. Comparison of pore pressure along the stimulated fracture at five moments of time for models I, II and III. Solid lines represent Model I in which permeability is manually changed in the whole fracture to reproduce the measurements at the injection well, dashed-lines represent Model II in which permeability changes according to the embedded model (Eq. (9)) and the fracture behaves elastically, and dotted-lines are for the viscoplastic Model III in which inelastic strain are taken into account

together with dilatancy that opens up the fracture as shear slip accumulates (see fracture profile in Figure 2).

Impact on nearby fractures

When stimulating a fracture, the perturbation is not limited to the fracture because (i) pore pressure diffuses through the low-permeability rock matrix (Figure 24), (ii) induced poromechanical strain-stress changes extend further away than the stimulated fracture (Figure 26) and (iii) shear slip stress transfer modifies the stress state around the slipped area of the fracture (Figure 29), which may either promote shear failure of nearby fractures or inhibit it (stress shadow). At BULGG, the stress of state leads to a shear stress acting on the fractures that is left-lateral. When shear slip occurs along a fracture, the stress drop is right-lateral (blue colours in Figure 29). The induced right-lateral shear stress is not limited to the slipped area and forms two lobes at the tips of the slipped area that affect portions of nearby, creating the so-called stress shadow, which inhibits shear slip of these regions. Thus, if subsequent hydraulic stimulations are performed in nearby fractures, the portions affected by the stress shadow may not be reactivated and permeability enhancement would be limited. On the contrary, the areas affected by the yellow-reddish colours in Figure 29 experience a left-lateral shear stress that favours subsequent fracture reactivation if these fractures are stimulated. Note that the fractures placed close to the stimulated fracture contain both areas where shear slip is promoted and inhibited.

To illustrate the abovementioned described effect, Figure 38 displays the trajectories of the deviatoric stress, *q*, versus the effective mean stress, *p'*, at eight points located in nearby fractures. For comparison purposes, all the axes have the same range of values. The failure surface is not plotted because it is placed to the left of the plotted values, i.e., all points are stable during the whole stimulation. Some areas are barely affected by stimulation (points 1 and 2). In contrast, others experience significant stress changes (up to 3 MPa both in deviatoric and effective mean stress) despite injection occurs in a nearby fracture and not within the fracture containing the point (points 4, 5 and 6). The trajectories are diverse, which highlights the complexity of the pore pressure and stress changes that occur not only within the stimulated fracture, but also in its surroundings. Some points approach shear failure conditions, either because of an increase in the deviatoric stress (point 1), a decrease in the effective mean stress (point 7) or a combination of both (point 4). Shear failure conditions are also approached by a decrease in the effective mean stress accompanied by a slight decrease in the deviatoric stress (point 5 after 1.5 h of stimulation), which is usually the case when elastic poromechanical stress changes occur as a result of pore pressure increase (Vilarrasa et al., 2019). Yet, the trajectory at point 5 is more complex, showing an initial increase in deviatoric stress at constant effective mean stress, followed by a decrease in the deviatoric stress and effective mean stress, which could have been caused by shear slip stress transfer and subsequent slip-driven pore pressure changes (Vilarrasa et al., 2021). Other sharp changes in the deviatoric stress are also induced by reactivation of the stimulated fracture (see points 4 and 6). Other areas, affected by the stress shadow, move away from the failure surface (points 3 and 8).

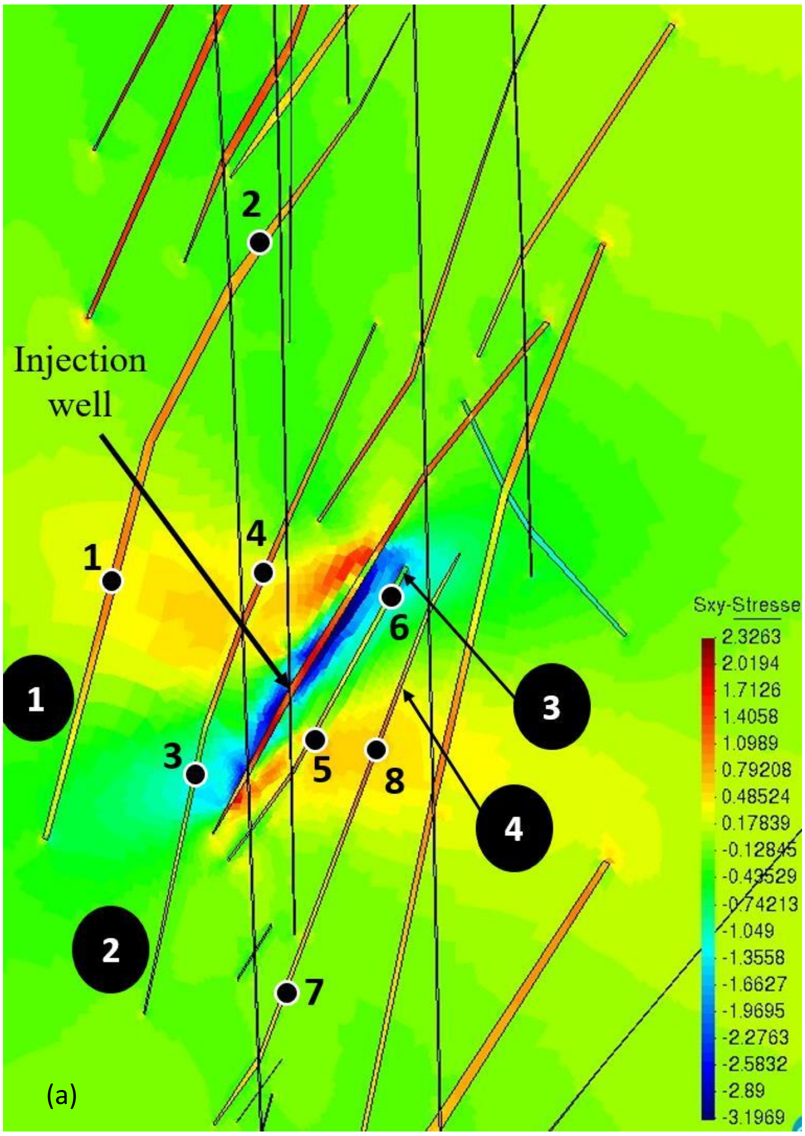
Injection well
1
2
3
4
5
6
7
8
Sxy-Stresse
2.3263
2.0194
1.7126
1.4058
1.0989
0.79208
0.48524
0.17839
-0.12845
-0.43529
-0.74213
-1.049
-1.3558
-1.6627
-1.9695
-2.2763
-2.5832
-2.89
-3.1969
(a)

564

565

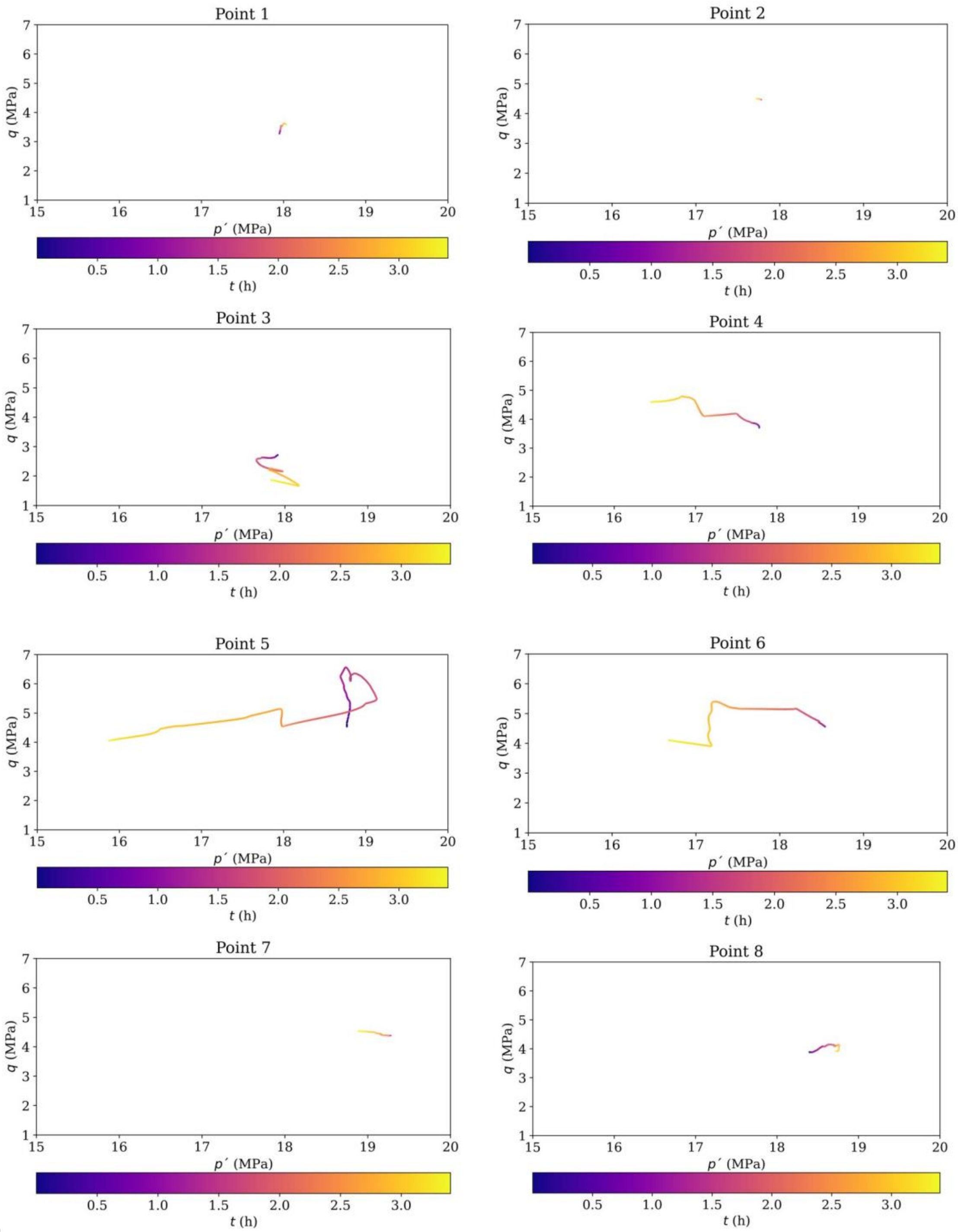

(b)

Figure 38. (a) Location of the points within four nearby fractures to the stimulated fracture, with the shear stress after 3.4 h in the background. (b) Trajectories of deviatoric stress (q) versus effective mean stress (p') at the eight indicated in (a).

4. Conclusions

We have numerically modelled one of the hydraulic stimulations performed at the BULGG using three different approaches. The first approach, in which the permeability of the stimulated fracture is manually changed to reproduce the overpressure measured at the field in response to injection, does a reasonable job in terms of curve fitting. However, since the permeability is homogeneously changed all along the fracture, the pore pressure distribution and associated poromechanical response of the rock are not well captured. The second approach uses the embedded model to calculate permeability changes as a function of volumetric strain, which, in turn, depends on pore pressure build-up. In this approach, the fracture is considered to be elastic during the whole stimulation. The temporal evolution of overpressure at the injection borehole is very well captured at the early stages of stimulation, but it is overestimated subsequently. The divergence between simulation results and field measurements coincide with the time at which the fracture yields, significantly opening up the fracture due to dilation (i.e., potential jacking). To reproduce the post-failure behaviour, the third approach is like the second one in terms of computing the permeability enhancement, but incorporates viscoplasticity with strain weakening and dilatancy. Dilatancy results in an additional enhancement of fracture permeability by one order of magnitude that renders a very good fit of field measurements. Simulation results show that permeability enhancement is achieved along 40 m of the fracture after 3.4 hours of hydraulic stimulation. Notably, the overall permeability enhancement is permanent, despite some minor permeability drops are observed during shut-in cycles.

5. References

Olivella, S., Carrera, J., Gens, A., & Alonso, E. E. (1994). Non-isothermal multiphase flow of brine and gas through saline media. *Transport in Porous Media*, *15*(3), 271-293.

Olivella, S., Gens, A., Carrera, J., & Alonso, E. E. (1996). Numerical formulation for a simulator (CODE_BRIGHT) for the coupled analysis of saline media. Engineering Computation, 13(7), 87-112.

Olivella, S., & Alonso, E. E. (2008). Gas flow through clay barriers. Géotechnique, 58(3), 157-176.

Vilarrasa, V., Carrera, J., Olivella, S., Rutqvist, J., & Laloui, L., 2019. Induced seismicity in geologic carbon storage. Solid Earth, 10, 871-892.

Vilarrasa, V., De Simone, S., Carrera, J., & Villaseñor, A., 2021. Unravelling the causes of the seismicity induced by underground gas storage at Castor, Spain. Geophysical Research Letters, 48, e2020GL092038.

Witherspoon, P. A., Wang, J. S., Iwai, K., & Gale, J. E. (1980). Validity of cubic law for fluid flow in a deformable rock fracture. Water Resources Research, 16(6), 1016-1024.

Zimmerman R. (2000). Coupling in poroelasticity and thermoelasticity. International Journal of Rock Mechanics and Mining Sciences, 37(1-2):79-87.